# Synthesis, Structure, and Spectroscopy of Rare Earth Hypophosphites. 1. Anhydrous and Monohydrated Lanthanide Hypophosphites

**Peter A. Tanner,*[,1a] Michele D. Faucher,[1b] and Thomas C. W. Mak[1c]**

Department of Biology and Chemistry, City University of Hong Kong, Tat Chee Avenue, Kowloon, Hong Kong SAR, UMR 8580 du CNRS, "Structures, Proprietes et Modelisation des Solides", Ecole Centrale Paris, 92295 Châtenay-Malabry Cedex, France, and Department of Chemistry, The Chinese University of Hong Kong, Shatin, New Territories, Hong Kong SAR

*Received February 17, 1999*

The lanthanide hypophosphite complexes $Ln(H_2PO_2)_3$ (Ln = La, Pr, Nd) and $Ln(H_2PO_2)_3 \cdot H_2O$ (Ln = La, Pr) crystallize in the space group $P\bar{1}$ (No. 2), $Z = 2$. The lattice constants for $La(H_2PO_2)_3$ are $a = 6.7912(6)$ Å, $b = 7.0801(8)$ Å, $c = 8.863(1)$ Å, $\alpha = 82.64(1)°$, $\beta = 74.43(1)$ °, $\gamma = 71.91(1)°$; for $La(H_2PO_2)_3 \cdot H_2O$, $a = 7.2291(4)$ Å, $b = 7.983(1)$ Å, $c = 8.934(1)$ Å, $\alpha = 110.57(1)°$, $\beta = 98.26(1)°$, $\gamma = 104.35(1)°$. In both structures hypophosphite ions bridge adjacent 8-coordinate lanthanide ions to give infinite chains. Infrared and Raman spectra (300−20 K) are shown to be consistent with the crystallographic data, with 52 of the 54 fundamental hypophosphite modes of vibration assigned. The electronic spectra of the anhydrous compounds consist mainly of bands due to pure electronic electric dipole transitions. Two-center vibronic transitions observed in the $^3H_4 \rightarrow {}^1D_2$ spectrum of $Pr(H_2PO_2)_3$ are not well-simulated by a model with dipole−dipole interaction terms between the two centers. The energy level scheme of $Pr^{3+}$ in $Pr(H_2PO_2)_3$ was fitted to a model Hamiltonian for a $C_{2v}$ site symmetry $Pr^{3+}$ ion, including configuration interaction of $4f^2$ with 4f6p. Theoretical crystal field parameters were in reasonable agreement with those derived from the energy level fitting. The results highlight the $C_{2v}$ $B_0^k$ ($k$ even) and $C_1$ $B_q^k$ ($k$ odd) distortions from the ideal $D_{4d}$ antiprismal structure, which slightly modify the $4f^2$ energy level scheme, and largely determine the spectral intensities in $Pr(H_2PO_2)_3$, respectively. The derived energy level scheme of $Nd(H_2PO_2)_3$ is similar to that for 8-coordinated $Nd^{3+}$ in $NdCl_3 \cdot 6H_2O$.

## 1. Introduction

There have been some conflicting conclusions from spectroscopic studies, on the one hand, and structural studies, on the other, of the structure and bonding in the metal complexes of the hypophosphite (phosphinate, or dihydrodioxophosphate(I)) anion. For example, from vibrational spectroscopic studies, a one-center bidentate coordination of $H_2PO_2^-$ was envisaged in the mononuclear complex $VO(H_2PO_2)_2 \cdot H_2O$,[2] in the binuclear complex $[Mo_2O_4(H_2PO_2)_2(H_2O)_2]$,[3] and also in the proposed structure $Ni(H_2PO_2)_2^+ \cdot (H_2PO_2)^-$ for nickel(II) hypophosphite.[4] Cation effects upon one-bond P−H coupling constants in $H_2PO_2^-$ in $^{31}P$ NMR spectra were interpreted using a model in which the anion has bidentate coordination to a metal ion.[5] However, crystallographic studies have shown that $(H_2PO_2)^-$ acts not as a chelating ligand but as a bridging ligand between cations via one or both oxygens.[6] The first objective of the present study was therefore to show that crystallographic and vibrational spectroscopic data for hypophosphite complexes can be reconciled. This has been demonstrated in detail for the cases of lanthanide hypophosphites, and it turns out that the vibrational data are more sensitive and informative of changes in P−H bond distances than X-ray data. We have published a preliminary account of the room-temperature Raman spectra elsewhere.[7]

A range of hypophosphite complexes have previously been studied by X-rays, and it is worthwhile to summarize the structural results. In $NH_4H_2PO_2$,[8] $KH_2PO_2$,[9] $CaNa(H_2PO_2)_3$,[10] $Mg(H_2PO_2)_2 \cdot 6H_2O$,[11] $NaH_2PO_2 \cdot {}^4/_5H_2O$,[12] $Zn(H_2PO_2)_2 \cdot xH_2O$ ($x = 0, 1$),[13,14] and $Ca(H_2PO_2)_2$,[15] the hypophosphite anion moeity is characterized by a distorted tetrahedral structure, the O−P−O and H−P−H angles being larger and smaller, respectively, than 109.47°, while the O−P−H angles are close to that value. The P−O bond distances are between 1.48 and 1.52 Å. The P−H distances reported from the neutron diffraction study of $Ca(H_2PO_2)_2$,[15] and also from the X-ray diffraction studies of $Zn(H_2PO_2)_2 \cdot xH_2O$[13] and $NaH_2PO_2 \cdot {}^4/_5H_2O$,[12] are less accurate and span a wider range between 1.21 and 1.48 Å, with the mean around 1.38 Å. Generally, the mean P−O bond distance (Å) increases as the O−P−O angle (in degrees) decreases, with the linear regression from the above 6-coordinate complexes being

$$\text{O−P−O} = 486.10 - 246.32\ \text{P−O}; \quad N = 8; \quad R^2 = 0.729 \quad (1)$$

The central cations are octahedrally coordinated to oxygen atoms in the above $M^I$ and $M^{II}$ complexes, with the exception of

(1) (a) City University of Hong Kong. (b) Ecole Centrale Paris. (c) The Chinese University of Hong Kong.
(2) Baran, E. J.; Etcheverry, S. B.; Diemann, E. *Polyhedron* **1985**, *4*, 1711.
(3) Sastry, M. S.; Kulshreshtha, S. K. *Transition Met. Chem.* **1989**, *14*, 248.
(4) Bickley, R. I.; Edwards, H. G. M.; Gustar, R. E.; Tait, J. K. F. *J. Mol. Struct.* **1992**, *273*, 61.
(5) Spitz, F. R.; Cabral, J.; Haake, P. *J. Am. Chem. Soc.* **1986**, *108*, 2802.
(6) Weakley, T. J. R. *Acta Crystallogr.* **1978**, *B34*, 281.
(7) Tanner, P. A.; Shamir, J.; Starostin, P. *J. Mol. Struct.* **1994**, *326*, 267.
(8) Zachariasen, W. H.; Mooney, R. C. L. *J. Chem. Phys.* **1934**, *2*, 34.
(9) Akimoto, T. B.Sc. Thesis, University of Tokyo, Japan, 1965 (in Japanese, not available to us).
(10) Matsuzaki, T.; Iitaka, Y. *Acta Crystallogr.* **1969**, *B25*, 1932.
(11) Galigné, J. L.; Dumas, Y. *Acta Crystallogr.* **1973**, *B29*, 1115.
(12) Catti, M. *Acta Crystallogr.* **1979**, *B35*, 1041.
(13) Tanner, P. A.; Liu, Y.-L.; Mak, T. C. W. *Polyhedron* **1997**, *16*, 495.
(14) Weakley, T. J. R. *Acta Crystallogr.* **1979**, *B35*, 42.
(15) Loopstra, B. O. *Jt. Estab. Nucl. Energy Res. Rep.* **1958**, Publ. no. 15, 64.

10.1021/ic990187z CCC: $18.00 
Published on Web 11/30/1999

$NH_4H_2PO_2$, where each oxygen of the hypophosphite forms acceptor hydrogen bonds at 2.81 Å from two nitrogen atoms, forming part of a tetrahedral arrangement around each one. In the double salt, $CaNa(H_2PO_2)_3$, each oxygen of the hypophosphite group is coordinated octahedrally to both Ca and Na.[10] The hypophosphite anion plays a rather different role in the structure of $Mg(H_2PO_2)_2 \cdot 6H_2O$, each oxygen being hydrogen-bonded to three molecules of water of three different $[Mg(H_2O)_6]^{2+}$ octahedra.[11] $Zn(H_2PO_2)_2$ has a polymeric layer-type structure, whereas $Zn(H_2PO_2)_2 \cdot H_2O$ forms a three-dimensional polymeric network, with both Zn−O−Zn and Zn−O−P−O−Zn bridges.[13,14] In anhydrous $U(H_2PO_2)_4$, hypophosphite anions again serve as bridging groups in linking the uranium centers to yield a three-dimensional network, but the coordination geometry of uranium is approximately square antiprismal.[16]

Structures of some complexes involving other ligands in addition to hypophosphite have been investigated. In the isostructural compounds $U(H_2PO_2)_3X \cdot 2H_2O$ (X = Cl, Br),[17a,b] the oxygen atoms of the hypophosphite anion occupy ligand sites around the uranium(IV) ion, as part of its distorted tetragonal antiprism environment. The uranium coordination polyhedra and hypophosphite tetrahedra are linked through these common oxygens to form thick layers in the resulting crystal structure. The layer structures of $MCl(H_2PO_2) \cdot H_2O$ (M = Co,[18] Ni[19]) consist of $H_2PO_2^-$ bridges between distorted octahedral dimers comprising two $[MO_3Cl_2(H_2O)]^{6-}$ sharing an edge of O atoms. The M−O−P−O−M bridges are a common feature in polymeric $Mn(H_2PO_2)_2 \cdot (C_{12}H_8N_2)$,[20] chain-structured $MCl(H_2PO_2)$ (M = Sn, Ge),[21] and chain-structured $Mn(H_2PO_2)_2 \cdot (C_{10}H_8N_2)$.[6]

The comparison of these hypophosphite structures comprising divalent and tetravalent cations with those of trivalent lanthanide ions appeared to be worthwhile, and the second objective of the present study was to synthesize these compounds in anhydrous and hydrated crystalline forms. We subsequently became aware of previous X-ray diffraction studies of $Ln(H_2PO_2)_3 \cdot H_2O$ (Ln = La, Eu),[22] but although the crystallographic results are consistent with the present study, the photographic data were of poor precision. The crystal structure of $Pr(H_2PO_2)_3$ has been reported by Seddon et al.,[23] following our preliminary communication.[7] Since the precision is similar to ours, we only report herein the crystallographic data for $La(H_2PO_2)_3$ and $La(H_2PO_2)_3 \cdot H_2O$. During the course of revision of this manuscript, Seddon et al.[24] have classified the members of the series $[Ln(H_2PO_2)_3(H_2O)_n]$ (Ln = La−Tb, $n = 1$; Dy−Lu, $n = 0$) into four different structural types. The structures of $La(H_2PO_2)_3(H_2O)$ and $La(H_2PO_2)_3$ reported herein may be classified under two of these types, whereas the isostructural $Dy(H_2PO_2)_3$,[24] $Er(H_2PO_2)_3$,[25] and $Yb(H_2PO_2)_3$[26] belong to the third type. Reports of the phosphite complexes $Ln_2(HPO_3)_3 \cdot xH_2O$ (Ln = lanthanide; $x = 1, 1.5, 2-4$)[27] and mixed phosphite−hypophosphite complexes $[Ln(H_2PO_2)(HPO_3)(H_2O)_n] \cdot xH_2O$[24] have been given.

The third objective of this study aimed to utilize the sharp intraconfigurational f−f spectra of praseodymium(III) in order to study (i) the crystalline environment of $Pr^{3+}$, enabling the refinement of the crystal field model; and (ii) the two-center transitions involving simultaneous excitation of the lanthanide ion and of vibrations of $H_2PO_2^-$. In these, the $Ln^{3+}$ ion acts as a structural probe of the vibrations of its local environment. Our interest in items i and ii rests upon the test of theory with experiment.

Objective i involved the fitting of the derived energy level scheme of $Pr^{3+}$ to a crystal field model in the case of low site symmetry. This was approached by the ab initio calculation of crystal field parameters, and the search for the highest symmetry model of the lanthanide ion which was compatible with experiment. In addition, the effects of the configuration interaction (CI) of $4f^2$ with $4f^16p^1$ [28−32] have been studied.

It was considered that the intensities of high-energy hypophosphite stretching vibrations in the electronic spectra would provide a useful test of Dexter−Stavola two-center vibronic transition theory.[33−37] It turned out that very weak features in the electronic absorption spectra of $Pr(H_2PO_2)_3$ due to $Nd^{3+}$ impurity obscured the regions of major interest. Nevertheless, some preliminary semiquantitative conclusions have been made concerning two-center vibronic transitions from the high-resolution, low-temperature electronic spectra.

The three objectives have now been attained through the syntheses of compounds $Ln(H_2PO_2)_3$ (Ln = La, Pr, Nd) and $Ln(H_2PO_2)_3 \cdot H_2O$ (Ln = La, Pr), the determination of the crystal structures using X-ray crystallography, and the study of the infrared, Raman, electronic absorption, and emission spectra down to 20 K.

## 2. Experimental Section

**2.1. Synthesis of Compounds.** The preparation of $La(H_2PO_2)_3 \cdot xH_2O$ ($x = 0, 1$) was carried out as follows. $La_2O_3$ (0.503 g) (99.99%, Strem Chemicals) was added to 25 $cm^3$ of 50% $H_3PO_2$ (Reidel-de-Haën, RG) solution at 70 °C. Concentrated hydrochloric acid was slowly added, with stirring, until complete dissolution was achieved. The mixture was evaporated on a water bath to a volume <5 $cm^3$, and a further 20 $cm^3$ of $H_3PO_2$ was added. The mixture was then left to evaporate at room temperature. Two distinct types of crystals formed in different preparations, needlelike or flat platelets, and mixtures were not obtained. The crystals were picked from the solutions, washed with distilled water, and air-dried. Infrared spectra showed that the former crystals were hydrated, whereas the latter were anhydrous. The water of crystallization

(16) Tanner, P. A.; Sze, T. H.; Mak, T. C.; Yip, W. H. *J. Crystallogr. Spectrosc. Res.* **1992**, *22*, 25.
(17) (a) Tanner, P. A.; Sze, T. H.; Mak, T. C. W.; Wang, R. J. *Polyhedron* **1992**, *11*, 817. (b) Tanner, P. A.; Silvestre, J. P. F.; Dao, N. Q. *New J. Chem.* **1993**, *17*, 263.
(18) Marcos, M. D.; Ibáñez, R.; Amorós, P.; Le Bail, A. *Acta Crystallogr.* **1991**, *C47*, 1152.
(19) Marcos, M. D.; Amorós, P.; Sapiña, F.; Beltrán-Porter, A.; Martínez-Máñez, R.; Attfield, J. P. *Inorg. Chem.* **1993**, *32*, 5044.
(20) Weakley, T. J. R. *Acta Crystallogr.* **1978**, *B34*, 3756.
(21) Weakley, T. J. R. *Acta Crystallogr.* **1979**, *B35*, 3023.
(22) Ionov, V. M.; Aslanov, L. A.; Rybakov, V. B.; Porai-Koshits, M. A. *Kristallografiya* **1973**, *18*, 403, 405 (in Russian).
(23) Seddon, J. A.; Jackson, A. R. W.; Kresinski, R. A.; Platt, A. W. G. *Polyhedron* **1996**, *15*, 1899.
(24) Seddon, J. A.; Jackson, A. R. W.; Kresinski, R. A.; Platt, A. W. G. *J. Chem. Soc., Dalton Trans.* **1999**, *13*, 2183.
(25) Aslanov, L. A.; Ionov, V. M.; Porai-Koshits, M. A.; Lebedev, V. G.; Kulikovski, B. N.; Gilyarov, O. N.; Novoderezhkina, T. L. *Izv. Akad. Nauk. SSSR Neorg. Mater.* **1975**, *11*, 96 (in Russian).
(26) Tanner, P. A.; Mak, C. S.-K.; Mak, T. C. W. In preparation (Part 3 of this series).
(27) Foulon, J.-D.; Tijani, N.; Durand, J.; Rafiq, M.; Cot, L. *Acta Crystallogr.* **1993**, *C49*, 1.
(28) Faucher, M.; Moune, O. K. *Phys. Rev.* **1997**, *B55*, 4150.
(29) Faucher, M.; Moune, O. K. *J. Alloys Compds.* **1997**, *250*, 306.
(30) Faucher, M.; Moune, O. K.; Garcia, D.; Tanner, P. *Phys. Rev.* **1996**, *B53*, 9501.
(31) Garcia, D.; Faucher, M. *J. Chem. Phys.* **1985**, *82*, 5554.
(32) Faucher, M.; Tanner, P. *Int. Conf. f-Elements*, **1997**, Paris, Sept 14−18, P2−20.
(33) Stavola, M.; Dexter, D. L. *Phys. Rev.* **1979**, *B20*, 1867.
(34) Stavola, M. *J. Lumin.* **1984**, *31/32*, 4549.
(35) Stavola, M.; Friedman, J. M.; Stepnoski, R. A.; Sceats, M. G. *Chem. Phys. Lett.* **1981**, *80*, 192.
(36) Stavola, M.; Isganiyis, L.; Sceats, M. G. *J. Chem. Phys.* **1981**, *74*, 4228.
(37) Dexpert-Ghys, J.; Auzel, F. *J. Chem. Phys.* **1984**, *80*, 4003.

**Table 1.** Data Collection and Processing Parameters for $Ln(H_2PO_2)_3 \cdot xH_2O$ ($x = 0$, 1) at 20 °C

| empirical formula | $La(H_2PO_2)_3$ | $La(H_2PO_2)_3 \cdot H_2O$ |
|---|---|---|
| fw | 333.9 | 351.9 |
| space group | $P\bar{1}$ (No. 2) | $P\bar{1}$ (No. 2) |
| unit cell params | | |
| $a$/Å | 6.7912(6) | 7.2291(4) |
| $b$/Å | 7.0801(8) | 7.983(1) |
| $c$/Å | 8.863(1) | 8.934(1) |
| $V$/Å$^3$ | 389.8(2) | 452.24(9) |
| α/deg | 82.64(1) | 110.57(1) |
| $\beta$/deg | 74.43(1) | 98.26(1) |
| $\gamma$/deg | 71.91(1) | 104.35(1) |
| $Z$ | 2 | 2 |
| density (calcd)/g cm$^{-3}$ | 2.845 | 2.584 |
| Mo Kα radiation, $\lambda$/Å | 0.710 73 | 0.710 73 |
| abs coeff/cm$^{-1}$ | 60.6 | 52.5 |
| $R_F$[a] | 0.022 | 0. 027 |
| $R_w$[b] | 0.027 | 0.034 |

[a] $R_F = \sum||F_o| - |F_c||/\sum|F_o|$. [b] $R_w = [\sum w(|F_o| - |F_c|)^2/\sum w^2|F_o|^2]^{0.5}$.

was not lost from $La(H_2PO_2)_3 \cdot H_2O$ on heating for 1 day at 150 °C, but was removed after heating at 200 °C for 5 h.

Phosphorus and lanthanum were determined by a Perkin-Elmer 1000 ICP-AES, and hydrogen by a Leco CHN analyzer, both using external calibration.

Found (calcd) % by mass for $La(H_2PO_2)_3$: La, 41.7 ± 2.7 (41.60); P, 25.3 ± 0.8 (27.83); H, 2.1 ± 0.1 (1.81).

Found (calcd) % by mass for $La(H_2PO_2)_3 \cdot H_2O$: La, 44.9 ± 0.7 (39.48); P, 25.5 ± 0.3 (26.41); H, 2.5 ± 0.1 (2.29).

Similar preparations utilizing $Pr_6O_{11}$ (99.99%, Berkshire Ores) instead of $La_2O_3$ gave products which the infrared spectra (and subsequent crystal structure determinations) showed to be isostructural with the corresponding lanthanum hypophosphite compounds. A check upon the composition of $Pr(H_2PO_2)_3$ by a JEOL T300 SEM-EDX instrument, using $Pr_6O_{11}$ as standard, showed the presence of Pr and P only and gave the found (calcd) ratio by mass of these elements as 1.54 ± 0.03 (1.52). The electronic absorption spectra of $Pr(H_2PO_2)_3$ indicated the presence of a trace impurity of Nd. This was confirmed by ICP-AES analysis, with the measured Nd concentration found to be 0.1% by mass, but the enhancement effects of the matrix upon the determined value were not investigated.

**2.2. Crystal Structure Determination.** The data collection and processing parameters for the complexes $La(H_2PO_2)_3$ and $La(H_2PO_2)_3 \cdot H_2O$ are given in Table 1. Intensities were collected at room temperature on a Siemens R3m/V diffractometer and processed using a learned procedure.[38] Empirical absorption corrections based on Ψ-scan data were also applied.[39]

All calculations were performed on a PC 486 with the SHELXTL-PC program package.[40] Direct methods yielded the positions of the lanthanum and other non-hydrogen atoms, and the hydrogen atoms were located from subsequent difference maps. All non-hydrogen atoms were subjected to anisotropic refinement, and the coordinates of the hydrogen atoms were also varied with preassigned isotropic temperature factors. Analytical expressions of neutral-atom scattering factors were employed, and anomalous corrections were also incorporated.[41] The final atomic coordinates and equivalent isotropic thermal parameters are given in Table 2.

**2.3. Spectroscopic Methods.** Infrared spectra (400/200−7200 cm$^{-1}$) were recorded at room temperature and liquid-nitrogen temperature using Bomem MB-120 and Perkin-Elmer PE-1650 spectrometers equipped with a Specac variable-temperature cell. Raman and optical emission spectra were recorded for $Pr(H_2PO_2)_3$ at 300 and 20 K, using the 457.9, 476.5, 488, and 514.5 nm lines of an argon ion laser and a Spex 1403-DM spectrometer. The absorption spectra of $Pr(H_2PO_2)_3$ were recorded between 300 and 20 K with a Biorad FTS-60A spectrometer, equipped with PbSe, Si, and photomultiplier detectors, and using an Oxford Instruments closed-cycle cooler cryostat. Preliminary experiments utilized pressed disks of $Pr(H_2PO_2)_3$, but polycrystalline samples were employed for later studies. Electronic absorption spectra of powder samples of $Nd(H_2PO_2)_3$ were recorded using fluorolube mulls between thin glass plates, using silver sol to provide thermal contact with the copper block. The spectra were calibrated in vacuum wavenumbers, using the lines from Ne, Cd, Na, and Hg lamps.

**Table 2.** Atomic Coordinates and Equivalent Isotropic Temperature Factors[a] (Å$^2$) for $La(H_2PO_2)_3$ and $La(H_2PO_2)_3 \cdot H_2O$

| atom | $x$ | $y$ | $z$ | $U_{eq}/U_{iso}$ |
|---|---|---|---|---|
| | | $La(H_2PO_2)_3$ | | |
| La(1) | 0.27079(1) | 0.57917(1) | 0.35710(1) | 0.0101(1) |
| P(1) | 0.10550(7) | 0.13564(6) | 0.31910(5) | 0.0151(1) |
| O(1) | 0.0731(2) | 0.3121(2) | 0.4145(1) | 0.0158(3) |
| O(2) | 0.2194(2) | −0.0651(2) | 0.3799(2) | 0.0209(4) |
| H(1A) | 0.2315 | 0.1644 | 0.1756 | 0.03 |
| H(1B) | −0.0941 | 0.01381 | 0.03152 | 0.03 |
| P(2) | 0.72015(7) | 0.77333(6) | 0.30114(5) | 0.0157(1) |
| O(3) | 0.6227(2) | 0.6130(2) | 0.3941(1) | 0.0168(3) |
| O(4) | 0.9599(2) | 0.7123(2) | 0.2427(2) | 0.0221(4) |
| H(2A) | 0.6603 | 0.9309 | 0.3932 | 0.03 |
| H(2B) | 0.6253 | 0.8428 | 0.1799 | 0.03 |
| P(3) | 0.68177(7) | 0.27654(7) | 0.06082(5) | 0.0171(1) |
| O(5) | 0.5208(2) | 0.2881(2) | 0.2173(1) | 0.0210(3) |
| O(6) | 0.5996(2) | 0.3057(2) | −0.0846(1) | 0.0205(4) |
| H(3A) | 0.8222 | 0.0913 | 0.0437 | 0.03 |
| H(3B) | 0.8072 | 0.3952 | 0.0562 | 0.03 |
| | | $La(H_2PO_2)_3 \cdot H_2O$ | | |
| La(1) | 0.16076(1) | 0.31820(1) | 0.37022(1) | 0.0145(1) |
| P(1) | 0.34828(6) | 0.68597(7) | 0.76934(5) | 0.0217(1) |
| O(l) | 0.1517(2) | 0.5719(2) | 0.6437(1) | 0.0197(3) |
| O(2) | 0.5253(2) | 0.6606(2) | 0.7081(2) | 0.0322(6) |
| H(1A) | 0.3418 | 0.6227 | 0.8920 | 0.03 |
| H(1B) | 0.3684 | 0.8729 | 0.8399 | 0.03 |
| P(2) | −0.03444(9) | −0.19286(8) | 0.08877(6) | 0.0288(2) |
| O(3) | 0.1148(3) | −0.0225(2) | 0.2255(2) | 0.0352(5) |
| O(4) | −0.0082(3) | −0.2397(3) | −0.0816(2) | 0.0393(7) |
| H(2A) | −0.2225 | −0.1882 | 0.0792 | 0.04 |
| H(2B) | −0.0391 | −0.3426 | 0.1294 | 0.04 |
| P(3) | 0.46721(7) | 0.72386(8) | 0.30940(6) | 0.0240(1) |
| O(5) | 0.2876(2) | 0.6354(2) | 0.3565(2) | 0.0261(4) |
| O(6) | 0.6679(2) | 0.7649(2) | 0.4142(2) | 0.0264(4) |
| H(3A) | 0.4571 | 0.8942 | 0.3163 | 0.04 |
| H(3B) | 0.4530 | 0.6281 | 0.1464 | 0.04 |
| O(1W) | −0.1108(2) | 0.1352(2) | 0.4579(2) | 0.0303(5) |
| H(1WB) | −0.1442 | 0.0219 | 0.4441 | 0.05 |
| H(1WA) | −0.1869 | 0.1818 | 0.5089 | 0.05 |

[a] For La, P, and O, $U_{eq}$ is defined as one-third of the trace of the orthogonalized **U** tensor. For H the exponent takes the form $-8\pi^2 U_{iso} \sin^2\theta/\lambda^2$.

## 3. Results and Discussion

**3.1. Crystal Structures.** The coordination environments of the lanthanum(III) ion in $La(H_2PO_2)_3$ and $La(H_2PO_2)_3 \cdot H_2O$ are compared in Figure 1a,b, and selected bond lengths and angles for these are listed in the caption. The coordination geometry about the lanthanum atom in the anhydrous complex may be described as a distorted square antiprism, being more regular in the hydrated complex. The mean La−O (ca. 2.52 Å) and P−O (1.50 Å) distances are very similar in the anhydrous and hydrated complexes. Although the mean P−O distance is essentially identical with that found in 8-coordinated $U(H_2PO_2)_4$,[16] the shorter mean U−O distance (2.36 Å) reflects the smaller ionic radius of $U^{4+}$.

(38) Diamond, R. *Acta Crystallogr.* **1969**, *A25*, 43.
(39) Kopfmann, G.; Huber, R. *Acta Crystallogr.* **1968**, *A24*, 348.
(40) Sheldrick, G. M. In *Crystallographic Computing 3: Data Collection, Structure Determination, Proteins and Databases*; Sheldrick, G. M., Kruger, C., Goddard, R., Eds.; Oxford University Press: New York 1985; p 175.
(41) Ibers, J. A., Hamilton, W. C., Eds. *International Tables for X-ray Crystallography*; Kynoch Press: Birmingham, U.K. (now distributed by Kluwer Academic Press: Dordrecht, The Netherlands), 1974; Vol. IV, pp 55, 99, 149.

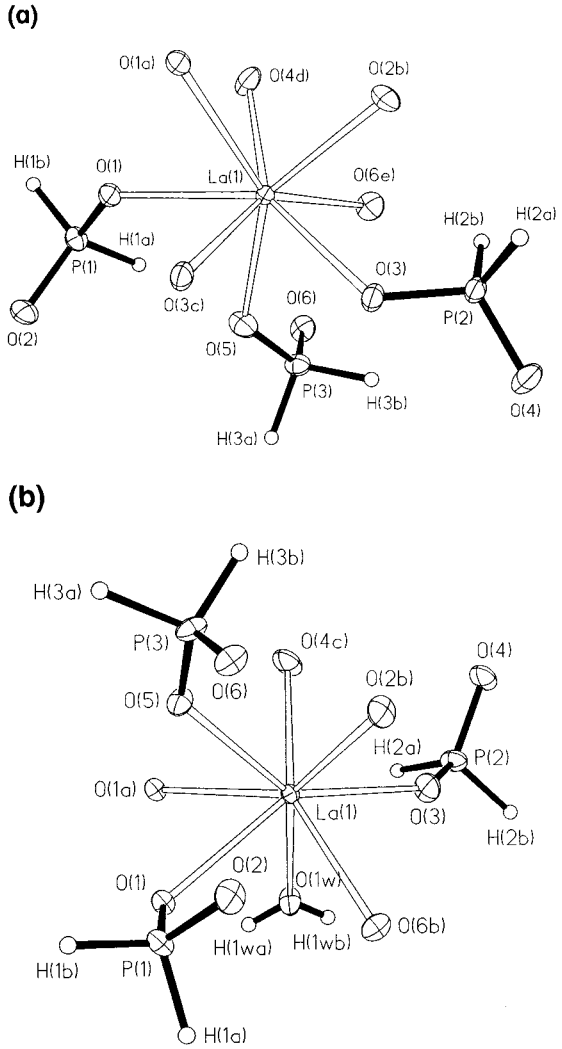


**Figure 1.** Thermal ellipsoid (35%) plot showing the atom-numbering scheme and the coordination geometry about the lanthanum atom in (a) $La(H_2PO_2)_3$ and (b) $La(H_2PO_2)_3{\cdot}H_2O$. (a) $La(H_2PO_2)_3$, selected bond lengths (Å) and angles (deg): La(1)−O(1) 2.569(1), La(1)−O(3) 2.583(1), La(1)−O(5) 2.453(1), La(1)−O(la) 2.625(1), La(1)−O(2b) 2.461(1), La(1)−O(3c) 2.591(1), La(1)−O(4d) 2.458(1), La(1)−O(6e) 2.464(1), P(1)−O(1) 1.525(1), P(1)−O(2) 1.501(1), P(2)−O(3) 1.530(1), P(2)−O(4) 1.508(1), P(3)−O(5) 1.511(1), P(3)−O(6) 1.504(2); O(1)−P(1)−O(2) 116.4(1), La(1)−O(1)−P(1) 129.4(1), O(3)−P(2)−O(4) 116.2(1), La(1)−O(3)−P(2) 120.9(1), O(5)−P(3)−O(6) 117.6(1), La(1)−O(5)−P(3) 130.0(1). Symmetry transformations: a ($-x$, $1-y$, $1-z$), b ($x$, $1+y$, $z$), c ($1-x$, $1-y$, $1-z$), d ($-1+x$, $y$, $z$), e ($1-x$, $1-y$, $-z$). (b) $La(H_2PO_2)_3{\cdot}H_2O$, selected bond lengths (Å) and angles (deg): La(1)−O(1) 2.592(1), La(1)−O(3) 2.475(2), La(1)−O(5) 2.524(2), La(1)−O(la) 2.621(1), La(1)−O(2b) 2.452(2), La(1)−O(4c) 2.442(2), La(1)−O(6b) 2.509(2), La(1)−O(lW) 2.537(2), P(1)−O(1) 1.512(1), P(1)−O(2) 1.495(2), P(2)−O(3) 1.495(1), P(2)−O(4) 1.490(2), P(3)−O(5) 1.506(2), P(3)−O(6) 1.500(2); O(1)−P(1)−O(2) 115.3(1), La(1)−O(1)−P(1) 116.1(1), O(3)−P(2)−O(4) 117.9(1), La(1)−O(3)−P(2) 138.1(1), O(5)−P(3)−O(6) 118.9(1), La(1)−O(5)−P(3) 131.9(1). Symmetry transformations: a ($-x$, $1-y$, $1-z$), b ($1-x$, $1-y$, $1-z$), *c* ($-x$, $-y$, $-z$), d ($-1+x$, $-1+y$, $z$).

In the crystal structure of $La(H_2PO_2)_3$, Figure 2a, all three independent $H_2PO_2^-$ ions each bridge a pair of adjacent metal atoms in the $\mu$(O,O′) mode to form a three-dimensional network. Furthermore, atom O(1) acts as a one-atom $\mu$(O,O) bridge, resulting in an infinite zigzag chain of centrosymmetric, corner-sharing $La_2O_2$ parallelograms [La(1)−O(1)−La(1a) 109.7(1)°, O(1)−La(1)−O(1a) 70.3(1)°] pointing in the *a* direction. In the crystal structure of $La(H_2PO_2)_3{\cdot}H_2O$, Figure 2b, which is also a three-dimensional network generated by bridging $H_2PO_2^-$

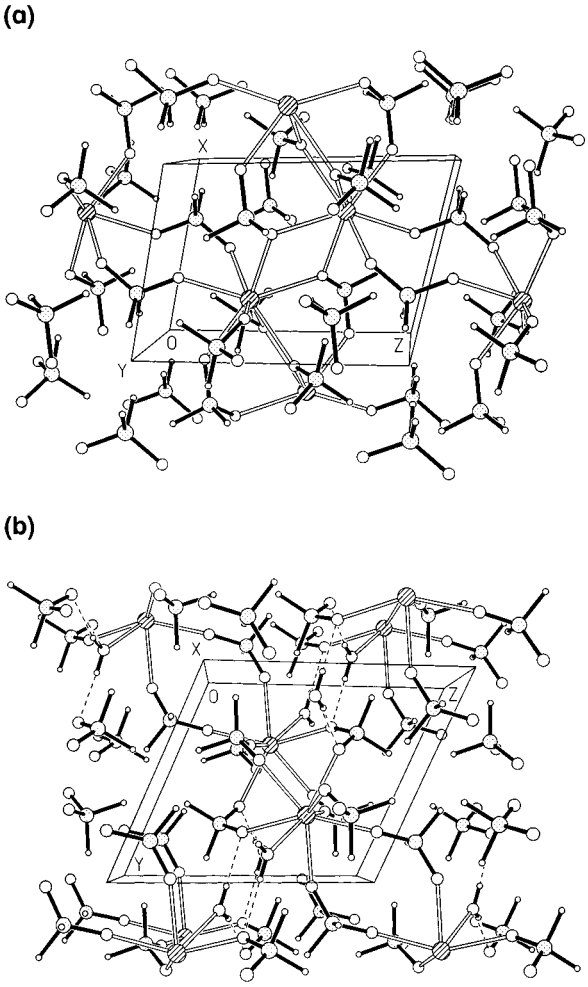


**Figure 2.** (a) Crystal structure of $La(H_2PO_2)_3$, viewed approximately parallel to the *b* axis. The metal ligand bonds are indicated by open lines. (b) Crystal structure of $La(H_2PO_2)_3{\cdot}H_2O$, viewed approximately parallel to the *a* axis. The metal−ligand and hydrogen bonds are represented by open and broken lines, respectively.

groups acting in an analogous manner, the $La_2O_2$ rings [La(1)−O(1)−La(1a) 115.3(1)°, O(1)−La(1)−O(1a) 64.7(1)°] centered at (0, $^1/_2$, $^1/_2$) are *not* directly linked to one another. The crystal structure is, however, consolidated by donor hydrogen bonds from the aqua ligand to its neighboring hypophosphite oxygen atoms [O(1W)···O(5a) 2.716(3) Å, O(lW)···O(6d) 2.849(3) Å].

The essential difference between the structures of the La and Pr complexes is the reduction in Ln−O bond distance by ca. 1.6% in the case of the smaller $Ln^{3+} = Pr^{3+}$ ion. The P−O bond distances are similar.

**3.2. Vibrational Spectra of $Ln(H_2PO_2)_3$, Ln = La, Pr, Nd.** The $C_{2v}$ symmetry hypophosphite ion possesses nine normal modes of vibration, all of which are Raman active and eight of which are infrared active. Deuteration studies,[42−44] the use of polarized radiation,[45,46] and normal coordinate analyses[43,44,47] have enabled firm assignments to be made for these modes of

(42) Abenoza, M.; Tabacik, V. *J. Mol. Struct.* **1975**, *26*, 95.
(43) Lovejoy, R. W.; Wagner, E. L. *J. Phys. Chem.* **1964**, *68*, 544.
(44) Ziomek, J. S.; Ferraro, J. R.; Peppard, D. F. *J. Mol. Spectrosc.* **1962**, *8*, 212.
(45) Tsuboi, M. *J. Am. Chem. Soc.* **1957**, *79*, 1351.
(46) Abenoza, M.; Hillaire, P.; Cadène, M. *C. R. Seances Acad. Sci., Ser. B* **1970**, *B271*, 346.
(47) Mayants, L. S.; Matrasov, E. I. *Izv. Akad. Nauk SSSR Neorg. Mater.* **1965**, *1*, 499.

**Table 3.** Vibrational Spectra of Solid-State Hypophosphite Complexes[a]

| | | wavenumber/cm$^{-1}$ at 300 K | | | |
|---|---|---|---|---|---|
| mode | $C_{2v}$ irrep | $KH_2PO_2$[b] | $La(H_2PO_2)_3$ | $Pr(H_2PO_2)_3$ | $Nd(H_2PO_2)_3$ |
| $\nu_4$ $PO_2$ | $a_1$ | 475 | R475sh, 486ms | R476m, 486ms | |
| scissor | | | IR471m, 484ms | IR473m, 487ms, 493sh | IR474m, 489s, 495sh |
| $\nu_7$ $PH_2$ | $b_1$ | 810 | R825m, 835mw | R824m, 836m, (842) | |
| rock | | | IR810ms, 821s, 832ms | IR812ms, 821ms, 833m | IR812ms, 822ms, 834ms |
| $\nu_5$ $PH_2$ | $a_2$ | 924 | R922m, 935ms, 950ms | R920m, 940ms, 954ms | |
| twist | | | IR920w | IR920w, 934vw, 947vw | IR918w, 936vw, 949vw |
| $\nu_3$ $PO_2$ | $a_1$ | 1050 | R1018m, 1030m, 1060s | R1018m, 1028m, 1058s | |
| sym str | | | IR999m, 1027m, 1044m | IR1000m, 1025m, 1042m | IR1001m, 1024m, 1041m |
| $\nu_9$ $PH_2$ | $b_2$ | 1081 | R1085m, 1105mw | R1080mw, 1084m, 1102mw | |
| wag | | | IR1081m, 1088m, 1099m | IR1080m, 1086m, 1098mw | IR1081m, 1087m, 1100m |
| $\nu_2$ $PH_2$ | $a_1$ | 1171 | R1126ms, 1135m, 1142mw | R1124ms, 1132m, 1140m | |
| scissor | | | IR1130s, 1147vs | IR1129vs, 1139w,[c] 1143vs | 1131vs, 1141vs |
| $\nu_8$ $PO_2$ | $b_2$ | 1230 | R1150m, 1162s | R1146m, 1160s | |
| ant. str | | | IR1160s, 1185s | IR1160s, 1170s,[c] 1182bs | 1157s, 1181s |
| $\nu_6$ $PH_2$ | $b_1$ | 2320 | R2360ms, 2366s | R2310vw,[d] 2366ms, 2374s | |
| ant str | | | IR2302w, 2349s, 2363ms | IR2305vw, 2354s, 2369ms | IR2304w, 2357s, 2371m |
| $\nu_1$ $PH_2$ | $a_1$ | 2345 | R2384s, 2416s, 2431m | R2386s, 2424vs, 2442m | |
| sym str | | | IR2378ms, 2410s, 2427m | IR2382ms, 2420s, 2434ms | IR2384m, 2424s, 2438m |

[a] Irrep, irreducible representation; sym, symmetric; ant., antisymmetric; str, stretch; m, medium; w, weak; s, strong; v, very; sh, shoulder; b, broad; R, Raman; IR, infrared. Raman modes transform as $A_g$, and IR modes as $A_u$ irreps for the $C_i$ unit cell group. [b] Data from refs 42−45. [c,d] Additional bands are resolved (c) at 120 K and (d) at 20 K.

vibration, as exemplified for $KH_2PO_2$ in Table 3. Subsequent proposed changes in assignments[48] and neglect of the effects of the solid state[4] have been shown to be incorrect.[7,49]

The strongest features in the Raman spectra of $Pr(H_2PO_2)_3$ (Figure 3) are the symmetric $PO_2$ and $PH_2$ stretching bands, assigned near 1058 and 2424 cm$^{-1}$, respectively, and corresponding features in the infrared spectra appear with medium intensity. The strongest features in the infrared spectra correspond to the $PH_2$ scissor and the $PO_2$ antisymmetric stretch modes.

The hypophosphite compounds studied in this work each crystallize in the space group $P\bar{1}$, with two formula units in the Bravais cell. The hypophosphite site symmetry group at each of the three independent $H_2PO_2^-$ ions in the Bravais cell is $C_1$, and the unit cell group is $C_i = S_2$. At each site, each hypophosphite vibrational mode is therefore potentially active as one [$A_u$ ($C_i$)] infrared band, and as a further one [$A_g$ ($C_i$)] Raman band, with mutual exclusion. The symmetry coordinates of the $A_u$ (or $A_g$) modes at the different sites mix, leading to a total of $3A_g + 3A_u$ ($C_i$) modes for each parent hypophosphite mode. In Table 3, it is observed, in accordance with this, that three components are resolved in each of the infrared and Raman spectra (with mutual exclusion) for most of the vibrations of $Pr(H_2PO_2)_3$. Figure 4a shows the three unit cell group $PH_2$ rocking modes in the room-temperature infrared spectrum of $Pr(H_2PO_2)_3$.

The assignments for the fundamental P−H stretching modes are not straightforward, however, some 23 bands being observed in the infrared spectrum of $Pr(H_2PO_2)_3$ between 1964 and 2491 cm$^{-1}$ (Figure 4e,f and Table 4a). Only three $\nu_s(PH_2)$ and three $\nu_{as}(PH_2)$ unit cell group modes (i.e., a total of six bands) are expected in this region of the infrared spectrum. There is no evidence for the occurrence of a phase transition on cooling. Many of these bands shift to higher energy by 2−3 cm$^{-1}$ on cooling from room temperature to 120 K, and the lower temperature spectrum is more clearly resolved. The fundamentals were assigned on the basis of the following two arguments.

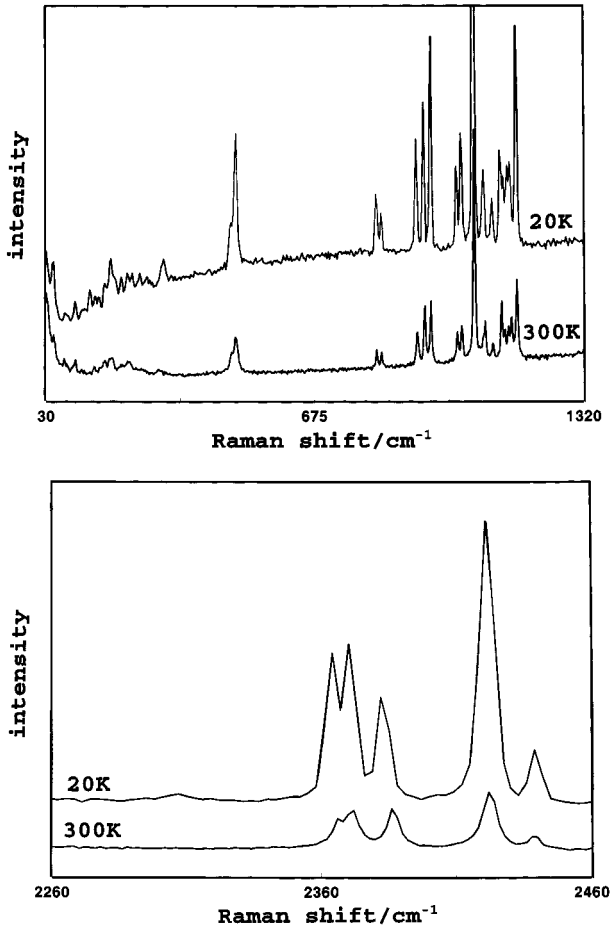


**Figure 3.** 514.5 nm excited Raman spectra of $Pr(H_2PO_2)_3$ at 300 and 20 K.

First, the weaker bands below 2350 cm$^{-1}$ in the infrared spectrum are assigned to $A_g + A_u$ combination bands mixed with the $A_u$ P−H stretch fundamentals. Since the highest energy P−O stretching fundamental modes are observed near 1182 cm$^{-1}$ in the infrared spectrum, and at 1160 cm$^{-1}$ in the Raman spectrum, Fermi resonances with the ($A_u$) $\nu_{as}(PH_2)$ modes may occur for combination bands of these modes. The lowest energy

(48) Bickley, R. I.; Edwards, H. G. M.; Knowles, A.; Tait, J. K. F.; Gustar, R. E.; Mihara, D.; Rose, S. J. *Spectrochim. Acta* **1994**, *50A*, 1277.
(49) Liu, R.; Moody, P. R.; Vanburen, A. S.; Clark, J. A.; Krauser, J. A.; Tate, D. R. *Vib. Spectrosc.* **1996**, *10*, 325.

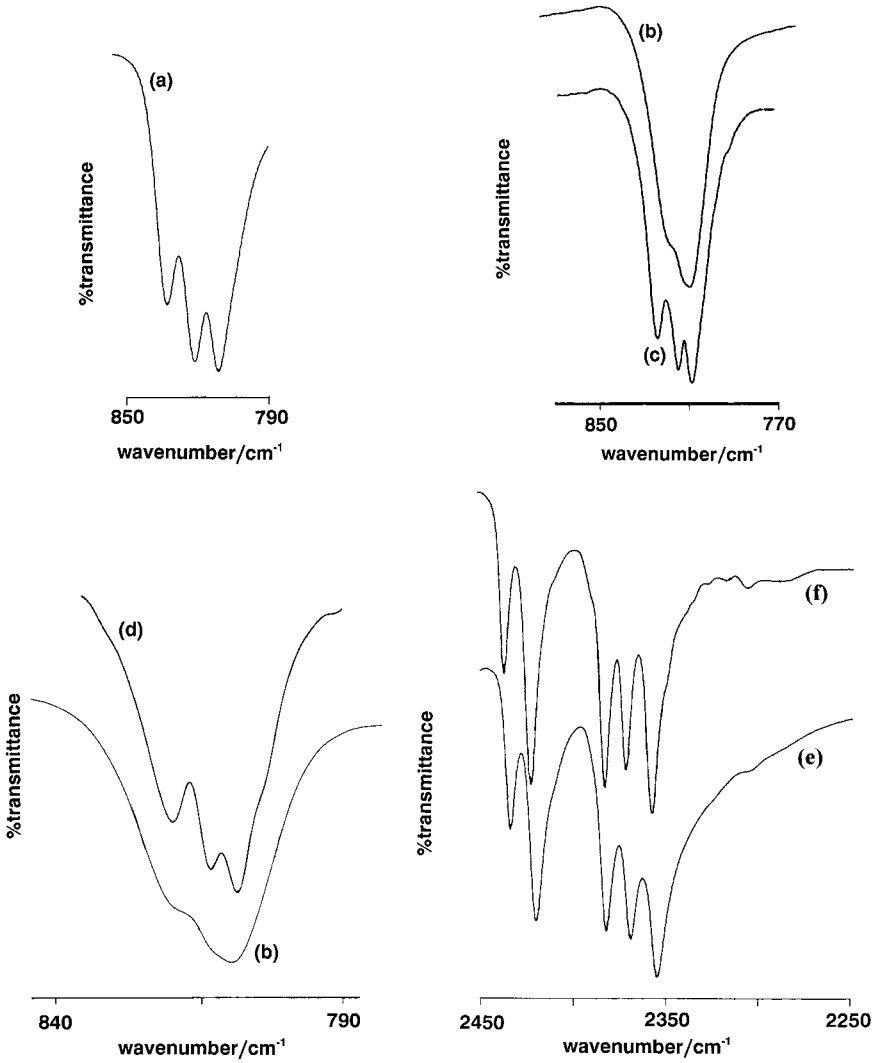


**Figure 4.** Infrared spectra: in the region of the P−H rocking mode (a) $Pr(H_2PO_2)_3$ at 300 K; (b) $La(H_2PO_2)_3{\cdot}H_2O$ at 300 K, and (c) at 120 K; (d) deconvoluted 300 K spectrum of $La(H_2PO_2)_3{\cdot}H_2O$; and in the region of the P−H stretching modes of $Pr(H_2PO_2)_3$ (e) at 300 K and (f) at 120 K.

$A_u$ P−H stretch is thus associated primarily with the weak band at 2305 $cm^{-1}$ in the 120 K infrared spectrum, but Fermi resonance occurs with several combination bands so that other weak features in this region have appreciable P−H stretch character (Table 4a). The prominent bands in the 120 K spectrum at 2356 and 2370 $cm^{-1}$ are assigned to the other two $\nu_{as}(PH_2)$ modes. The relative intensity pattern of these bands is repeated much more weakly at ca.100 $cm^{-1}$ to higher energy, being assigned to combinations involving the $A_g$ lattice vibration observed at 102 $cm^{-1}$ in the Raman spectrum (Table 4a). The three remaining intense infrared bands (at 2382, 2423, and 2437 $cm^{-1}$ at 120 K) are then assigned to the $\nu_s(PH_2)$ modes. The $A_g$ P−H stretching modes are assigned to six bands resolved in the 20 K Raman spectrum in this region. The lowest energy feature, at 2310 $cm^{-1}$, is very weak (Figure 3). Under this assignment scheme the higher energy group of bands corresponds to P−H symmetric stretching modes, and the lower to P−H antisymmetric stretching modes. The ungerade−gerade mode unit cell group splittings of the P−H stretching modes are then between 4 and 12 $cm^{-1}$, with the *total* unit cell group splittings of $\nu_{as}(PH_2)$ and of $\nu_s(PH_2)$ being similar (ca. 60 $cm^{-1}$), as measured in both the infrared and Raman spectra.

The second argument for the assignment of the P−H stretch fundamentals is concerned with the assignment of the bands between 4716 and 4870 $cm^{-1}$ in the infrared spectrum. To study these vibrational modes of $Pr(H_2PO_2)_3$, it is necessary to compare the spectrum with that of $La(H_2PO_2)_3$ because the $Pr^{3+}$ $^3H_6 \leftarrow {}^3H_4$ intraconfigurational electronic transitions overlap the vibrational combination bands (Figure 5). The vibrational bands in this region have been assigned (Table 4b) to combinations of gerade and ungerade unit cell group modes involving two quanta *only* of P−H stretch. The interpretation of the medium-intensity bands in the low-energy group would require an assignment involving three ungerade modes, or one ungerade and two gerade modes, or substantial intensity contribution away from the zone center *unless three modes* (labeled IR(a,b,c) in the footnote of Table 4b) of fundamental $A_u$ P−H stretch character have been assigned. Figure 5 also shows that the internal mode vibrational dispersion is small since the features are sharp and can be assigned to combinations of $\boldsymbol{k} = 0$ Raman ($A_g$) and infrared ($A_u$) modes.

From a molecular ion viewpoint, the appearance of the $PH_2$ twisting mode in the infrared spectrum of a hypophosphite complex would indicate that the site symmetry is lower than $C_{2v}$. In the present case, *if* the site symmetry *were* $C_{2v}$, then the unit cell group modes derived from this vibration would transform as $A_g$ ($C_i$) and have exclusive Raman activity. It may be concluded from the observation of the infrared bands between 920 and 950 $cm^{-1}$ in the spectrum of $Pr(H_2PO_2)_3$ (Table 3) that the hypophosphite ion site symmetry is $C_2$ or lower.

**Table 4.** Assignment of Infrared Combination Bands of $Pr(H_2PO_2)_3$ and $La(H_2PO_2)_3$

(a) $Pr(H_2PO_2)_3$ Bands between 1900 and 2500 $cm^{-1}$ at 120 K

| wavenumber/$cm^{-1}$ | assignment[a] |
|---|---|
| 1964w | IR812 + R1160 |
| 1977vw | IR822 + R1160; IR1160 + R824 |
| 2011vw | IR1086, 1098 + R920 |
| 2041vw | IR1086 + R954; IR1098 + R940 |
| 2089vw | IR947 + R1140, 1146 |
| 2162w | IR1080, 1086 + R1084, 1080 |
| 2243vw | IR1160 + R1080, 1084 |
| 2288bvw | IR1143 + R1146 |
| 2305w | IR1160 + R1146[b] |
| 2316vw | IR1160 + R1160[b] |
| 2326vw | IR1182 + R1146[b] |
| 2333sh | IR1170 + R1160 |
| 2348bsh | IR1182 + R1160 |
| 2356s | F |
| 2370ms | F |
| 2382s | F |
| 2409vw | IR2305 + R102 |
| 2423s | F |
| 2437ms | F |
| 2455vw | IR2356 + R102 |
| 2470vw | IR2370 + R102 |
| 2491vw | IR69(?) + R2422/combination band |

(b) $La(H_2PO_2)_3$ and $Pr(H_2PO_2)_3$ Combination Bands between 4600 and 4880 $cm^{-1}$ measured at 20 K[c]

| $La(H_2PO_2)_3$ | | $Pr(H_2PO_2)_3$ | | |
|---|---|---|---|---|
| line, Fig. 5 | wavenumber/$cm^{-1}$ | line, Fig. 5 | wavenumber/$cm^{-1}$ | assignment[d] |
| | | 1 | 4617bvw | IR(a) + R(a) |
| 2 | 4615m | 2 | 4626bm | IR(b) + R(a) |
| 3 | 4628ms | 3 | 4638ms | IR(c) + R(a) |
| 4 | 4649ms | 4a | 4663ms | IR(d) + R(a) |
| 5 | 4660w | 4b | 4669bw | IR(e) + R(a)<br>IR(a) + R(b) |
| 6 | 4677m | 6 | 4685mw | IR(f) + R(a)<br>IR(b) + R(b) |
| 7 | 4716m | 7 | 4729s | IR(d) + R(c) |
| 8 | 4725s | 8 | 4737s | IR(e) + R(b) |
| 9 | 4749s | 9 | 4757w | IR(e) + R(d)<br>IR(f) + R(c) |
| 10 | 4760ms | 10 | 4769s<br>4774m | IR(f) + R(d)<br>IR(d) + R(e) |
| 11 | 4779s | 11 | 4791s | IR(d) + R(f) |
| 12 | 4791s | 12 | 4804ms | IR(f) + R(e) |
| 13 | 4813w | 13 | 4824w | IR(h) + R(d) |
| 14 | 4831bw | 14 | 4847w | IR(g) + R(e) |
| 15 | 4852s | 15 | 4865s | IR(g) + R(f)<br>IR(h) + R(f) |

[a] Refer to footnote *a*, Table 3. F, fundamental mode. [b] These modes are strongly mixed with an $A_u$ fundamental mode. [c] Nr, not resolved at 300 K. Other abbreviations are given in footnote *a* below Table 3. Wavenumbers of corresponding bands in the spectra of $Nd(H_2PO_2)_3$ are 2−8 $cm^{-1}$ higher than in $Pr(H_2PO_2)_3$. [d] The wavenumbers of features observed in the P−H stretch region of the spectrum of $La(H_2PO_2)_3$ (measured at 300 K) and $Pr(H_2PO_2)_3$ (IR measured at 120 K, Raman at 20 K) are listed below. IR spectrum of $La(H_2PO_2)_3$ [$Pr(H_2PO_2)_3$]: (a) nr [2305]; (b) nr [2316]; (c) nr [2326]; (d) 2349 [2356]; (e) 2363 [2370]; (f) 2378 [2382]; (g) 2411 [2423]; (h) 2427 [2437]. Raman (R) spectrum: (a) nr [2310]; (b) 2360 [2367]; (c) 2366 [2373]; (d) 2384 [2385]; (e) 2416 [2424]; (f) 2431 [2442].

The $A_{1g}$ and $T_{1u}$ metal−oxygen stretching modes of $Mg(OH_2)_6^{2+}$ in crystalline magnesium hypophosphite have been assigned at 363 $cm^{-1}$ (Raman) and 430 $cm^{-1}$ (IR), respectively,[50] although the energies of $\nu_{as}(M^{II}-O[hyp])$ vibrations are somewhat lower.[13] The corresponding Pr−O stretching modes of the approximate archimedean antiprism, $PrO_8$, transform as $A_1$ and $E_1 + B_2$($D_{4d}$). The highest energy Pr−O modes in $Pr(H_2PO_2)_3$ are assigned to 300 K bands near 300 $cm^{-1}$ (Raman) and 340 $cm^{-1}$ (IR).

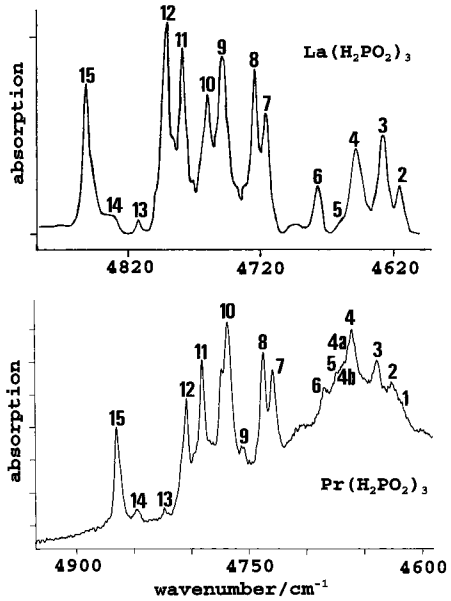


**Figure 5.** 20 K infrared spectra of $Ln(H_2PO_2)_3$ (Ln = La, Pr) between 4900 and 4590 $cm^{-1}$. The low-energy portion of the spectrum of $Pr(H_2PO_2)_3$ is overlapped by the $^3H_4 \rightarrow {}^3H_6$ electronic transition. Assignments are given in Table 4b.

The infrared spectra serve to confirm that the three anhydrous hypophosphites studied in this work are isostructural (Table 4). For the hypophosphite anion moiety, the detailed comparison of the *average* unit cell group mode energies at 300 K for X−P−X stretching (X = O, $\nu_3$, $\nu_8$; or X = H, $\nu_1$, $\nu_6$) and X−P−X bending (X = O, $\nu_4$; or X = H, $\nu_2$) in these spectra shows the shortening of P−O, opening of the O−P−O angle, lengthening of P−H, and closing of the H−P−H angle as the $Ln^{3+}$ ionic radius increases (i.e., as the Ln−O distance increases), as expected from Gutmann's first bond length variation rule.[51] Although the P−O bond distance changes are precisely determined, one is unable to discern small changes in the P−H bond distances from the X-ray studies. Vibrational spectroscopy is, however, a sensitive probe of these bond distance changes, with mean values of vibrational energies changing by several wavenumbers.[52]

**3.3. Vibrational Spectra of $Ln(H_2PO_2)_3 \cdot H_2O$ (Ln = La, Pr).** The $C_i$ unit cell group selection rules permit the appearance of three infrared and three Raman components for each parent hypophosphite vibration, and these are generally observed, although the spectra are more congested and not as clearly resolved as those of $Ln(H_2PO_2)_3$. For example, Figure 4b shows that two $PH_2$ rocking modes are resolved in the room-temperature infrared spectrum of $La(H_2PO_2)_3 \cdot H_2O$. Both the use of a lower temperature (Figure 4c) and the deconvolution of the room-temperature band shape (Figure 4d) indicate the presence of three features in this spectral region. For $La(H_2PO_2)_3 \cdot H_2O$, the $\nu_s$(P−H) bands are relatively weaker in the infrared spectrum, compared with those of $La(H_2PO_2)_3$, whereas the $\nu_{as}$(P−H) bands are relatively weaker in the Raman spectrum. The $PO_2$ scissor and the $PO_2$ antisymmetric stretch

(50) Abenoza, M.; Hillaire, P.; Lafont, R. *C. R. Seances Acad. Sci., Ser. B* **1971**, *B273*, 297.

(51) Gutmann, V. *The Donor-Acceptor Approach to Molecular Interactions*; Plenum: New York, 1978; p 7.

(52) Tanner, P. A. *J. Mol. Struct.* **1997**, *405*, 103.

both move to higher energy in the infrared spectra of $La(H_2PO_2)_3 \cdot H_2O$, compared with $La(H_2PO_2)_3$, attributed to hydrogen-bonding interactions. Several bands observed in the region below 700 $cm^{-1}$ of the infrared spectra of the hydrated hypophosphites sharpen at 120 K, and these features correspond to the librational modes of lattice water. The water stretching bands are observed with medium intensity at 3175 and 3402 $cm^{-1}$ in the infrared spectrum of $Pr(H_2PO_2)_3 \cdot H_2O$. The bending mode is observed as a single feature at 1650 $cm^{-1}$, with the first overtone at 3310 $cm^{-1}$, confirming the presence of only one type of water molecule in the unit cell of the hydrate. The water stretching modes appear weak in the Raman spectrum of $Pr(H_2PO_2)_3 \cdot H_2O$, at $3172 \pm 6$ and $3387 \pm 7$ $cm^{-1}$. The energies of these stretching modes are rather lower, and that of the bending mode higher, than the corresponding bands in the spectrum of $UCl(H_2PO_2)_3 \cdot 2H_2O$,[17a] attributed to stronger hydrogen bonding involving water.

**3.4. Electronic Absorption Spectra of $Pr(H_2PO_2)_3$.** The electronic ground state of the $f^2$ ion $Pr^{3+}$ is $^3H_4$, and the intraconfigurational transitions to all excited terms (with the exception of $^1S_0$ in this study) are accessible by ultraviolet−visible−near-infrared absorption spectrometry. The energy level assignments deduced from the spectral analyses are collected in Table 5, and selected spectra are shown in Figure 6. Under $C_1$ site symmetry, the $2J+1$-fold degeneracy of each $L_J$ term manifold is completely removed, with the representations of all crystal field levels being the same, $A(C_1)$. In this study, the crystal field components of a given term manifold are labeled A, B, C, ... in order of increasing energy. Davydov electronic energy level splittings were not resolved in the powder/polycrystalline spectra. The electronic transitions are expected to acquire considerable electric dipole intensity from the static mixing of opposite-parity wave functions by the crystal field. Thus all of the strong bands in the electronic spectra may be assigned to zero-phonon lines, and the location of the appropriate numbers of crystal field components of the terminal levels indicates that $Pr^{3+}$ occupies only one site of $C_2$ or lower symmetry. The exceptions to this are transitions to the $^1G_4$ (Figure 6a) and $^1D_2$ (Figure 6b) multiplet terms, discussed in section 3.6. The temperature dependence of the hot bands at 50 and 137 $cm^{-1}$ was studied at 35, 110−120, and 298 K and was particularly useful as a check in identifying weak zero-phonon lines. In particular, the transitions originating from the $(^3H_4)B$ level appeared as satellites at 50 $cm^{-1}$ to low energy of most zero-phonon lines, in many cases with oscillator strengths greater than the corresponding transitions from $(^3H_4)A$. For example, the transition to the $(^1D_2)D$ level from $(^3H_4)A$ is not observed at 20 K in Figure 6b, but the increase in relative intensity of $(^1D_2)D \leftarrow (^3H_4)B$ by a factor of 1.5 from 110 to 298 K enables the location of the D crystal field level.

**3.5. Emission Spectra of $Pr(H_2PO_2)_3$.** Spectra recorded using the 457.9 and 476.5 nm argon ion laser lines between 120 and 20 K, in the region between 20 800 and 13 200 $cm^{-1}$, showed weak emission bands, upon which were superimposed sharper features due to vibrational Raman scattering. The Raman scattering alone was excited by 488 or 514.5 nm excitation at 20 K. The strongest emission was observed from $^3P_0$ to the $^3H_{4,5,6}$ and $^3F_{2,3,4}$ term manifolds. The weak intensity of emission arises from the ability of P−H stretching modes to promote fast nonradiative decay from $^3P_0$ to lower energy term manifolds. A semiquantitative treatment involving the energy gap law has been given for $Pr(CH_3COO)_3 \cdot H_2O$,[53] in which water is a first-sphere ligand, where it was found that an efficient nonradiative cross-relation mechanism was operative for the $^1D_2$ state. Herein, it was found that the 77 K luminescence from $^3P_0$ in $Pr(H_2PO_2)_3 \cdot H_2O$, where water is a first-sphere ligand, is about 4 times weaker (relative to the Raman bands) than that from $Pr(H_2PO_2)_3$ because the $\nu(OH_2)$ mode effectively spans the gap $^3P_0-{}^1D_2$. Under blue excitation lines, the intensity of emission from $^1D_2$ was weak, but nevertheless provided confirmation of the energy level assignments from $^3P_0$ emission.

The assignments for the emission spectra enabled the locations to be determined for the $^3H_4$ and $^3H_5$ energy levels, which were largely inaccessible from absorption measurements, in addition to providing confirmatory assignments for higher crystal field levels. Strong features in the $^3P_0 \rightarrow {}^3H_4$ emission spectrum are assigned to transitions terminating on ground state levels located at 50, 137, 183, 359, and 538 $cm^{-1}$. The assignment of the three remaining $^3H_4$ levels was, however, not straightforward, because rather more than three weaker bands were apparent in the emission spectrum. This problem of the distinction between weak electronic transitions and vibronic transitions is illustrated for emission and absorption transitions terminating on $^3H_6$ in Figure 7, where the labels A−K identify the terminal crystal field levels of $^3H_6$. The final locations of energy levels were determined by a progressive refinement of the procedures: (i) comparison of experimental results with the calculated energy level scheme of $Pr^{3+}$ in $Pr(H_2PO_2)_3$; and (ii) further comparison of assignments in emission and absorption spectra, and the characterization of vibronic bands from vibrational data. The final experimental level assignments are collected in Table 5.

**3.6. Vibronic Transitions in the Electronic Spectra of $Pr(H_2PO_2)_3$: One-Center Transitions.** Because the LSJ-multiplet terms of $Pr^{3+}$ are fully split under the $C_1$ site symmetry, the large number of bands due to pure electronic transitions in the absorption and emission spectra of $Pr(H_2PO_2)_3$ largely masks weaker vibronic features. The most transparent regions, enabling vibronic structure to be identified up to ca. 300 $cm^{-1}$ from the zero-phonon line, are the absorption sidebands of $^3H_4 \rightarrow {}^1D_2$ and $^3H_4 \rightarrow {}^3P_0$. Various formalisms have been employed to account for the appearance of vibronic transitions in intraconfigurational f−f transitions of the electronic spectra of rare earth ions (see, for example, refs 54−57). Considering vibrations involving the central cation and nuclei within the first coordination sphere, in the weak-coupling limit the vibronic transition[54] involves vibronic coupling of the initial state to an intermediate fd or fg electron state, followed by an electric dipole allowed transition to the terminal state. Magnetic dipole vibronic sidebands may occur via two distinct mechanisms, but generally the intensity is very weak.[54] Vibronic processes involving totally symmetric progressions upon zero-phonon lines or vibronic origins are very weak in intraconfigurational f−f transitions, where potential energy hypersurfaces are similar for the states involved. The vibronic structure of the $^3P_0 \rightarrow {}^3H_4$ emission transition of $Pr(CH_3COO)_3 \cdot H_2O$ has been compared with bands in the corresponding low-temperature Raman spectrum,[53] but a correspondence of features may occur for pure electronic transitions in emission and electronic Raman transitions. For $Pr(H_2PO_2)_3$, some of the more intense bands below 450 $cm^{-1}$ in the 20 K Raman spectrum are not evident at room temperature

(53) Hehlen, M.-O.; Riesen, H.; Güdel, H. U. *Inorg. Chem.* **1991**, *30*, 2273.
(54) Henderson, B.; Imbusch G. F. *Optical Spectroscopy of Inorganic Solids*; Clarendon Press: Oxford, 1989; p 221.
(55) Piepho, S. B.; Schatz, P. N. *Group Theory in Spectroscopy*; John Wiley: New York, 1983; p 44.
(56) Cohen, E.; Moos, H. W. *Phys. Rev.* **1967**, *161*, 258.
(57) Ballhausen, C. J.; Hansen, A. E. *Annu. Rev. Phys. Chem.* **1972**, *23*, 15.

**Table 5.** Energy Levels of $Pr^{3+}$ in $Pr(H_2PO_2)_3$

| term manifold cryst field level label[a] | exptl energy | | fitted energy[b] | calcd energy with CI[c] | $\Delta$[d] | | $C_{2v}$ irrep |
|---|---|---|---|---|---|---|---|
| | absorption | emission | | | with CI | without CI[e] | |
| $^3H_4$ A | 0 | 0 | 0 | −2 | 2 | −20 | $B_2$ |
| B | 50 | 50 | 50 | 44 | 6 | 8 | $B_1$ |
| C | 138 | 137 | 137 | 146 | −9 | −29 | $A_2$ |
| D | 185 | 183 | 184 | 190 | −6 | 9 | $A_1$ |
| E | | (214) | 214 | 238 | −24 | −17 | $B_1$ |
| F | | (310) | 310 | 301 | 9 | 0 | $A_1$ |
| G | | 359 | 359 | 363 | −4 | 10 | $B_2$ |
| H | | 538 | 538 | 524 | 15 | 17 | $A_2$ |
| I | | 538 | 538 | 541 | −3 | 8 | $A_1$ |
| $^3H_5$ A | | 2204 | 2204 | 2207 | −3 | −22 | $B_1$ |
| B | | 2231 | 2231 | 2227 | 4 | 0 | $A_1$ |
| C | | 2256 | 2256 | 2251 | 5 | 12 | $A_2$ |
| D | | | | 2252 | | | $B_2$ |
| E | | 2304 | 2304 | 2295 | 9 | −2 | $B_2$ |
| F | | (2307) | | 2312 | | | $A_2$ |
| G | | (2321) | | 2345 | | | $A_1$ |
| H | | 2440 | 2440 | 2430 | 10 | 23 | $B_1$ |
| I | | | | 2482 | | | $A_2$ |
| J | | 2648 | 2648 | 2634 | 14 | 21 | $B_2$ |
| K | | 2648 | 2648 | 2637 | 11 | 19 | $B_1$ |
| $^3H_6$ A | 4344 | 4344 | 4344 | 4358 | −14 | 30 | $A_1$ |
| B | 4349 | 4348 | 4349 | 4362 | −13 | −35 | $A_2$ |
| C | 4387 | 4384 | 4386 | 4371 | 15 | −3 | $B_1$ |
| D | 4397 | 4393 | 4396 | 4387 | 9 | −5 | $B_2$ |
| E | 4422 | 4420 | 4421 | 4449 | −28 | −18 | $B_2$ |
| F | (4474) | 4474 | 4474 | 4477 | −3 | 11 | $A_1$ |
| G | 4493 | (4488) | 4493 | 4493 | 0 | −3 | $B_1$ |
| H | 4535 | (4538) | 4536 | 4536 | −1 | −8 | $A_2$ |
| I | | (4608) | | 4568 | | | $B_1$ |
| J | 4661 | 4668 | 4661 | 4656 | 5 | 10 | $A_1$ |
| K | (4674) | 4668 | 4674 | 4669 | 5 | 20 | $B_2$ |
| L | (4983) | 4984 | 4983 | 4977 | 6 | 16 | $A_1$ |
| M | 4987 | 4984 | 4987 | 4978 | 10 | 20 | $A_2$ |
| $^3F_2$ A | 5094 | 5092 | 5093 | 5092 | 1 | −12 | $A_2$ |
| B | 5117 | 5116 | 5117 | 5114 | 3 | 5 | $B_2$ |
| C | 5133 | 5132 | 5133 | 5129 | 4 | 21 | $A_1$ |
| D | 5143 | 5144 | 5144 | 5151 | −7 | −36 | $B_1$ |
| E | 5243 | 5244 | 5243 | 5266 | −23 | −4 | $A_1$ |
| $^3F_3$ A | 6453 | 6453 | 6453 | 6453 | 0 | −4 | $B_2$ |
| B | 6476 | 6477 | 6476 | 6474 | 2 | 8 | $B_1$ |
| C | 6490 | 6489 | 6490 | 6487 | 3 | 13 | $A_2$ |
| D | 6505 | 6505 | 6505 | 6497 | 8 | 4 | $A_1$ |
| E | 6526 | 6525 | 6526 | 6521 | 5 | −6 | $B_1$ |
| F | 6546 | (6549) | 6546 | 6541 | 5 | −2 | $B_2$ |
| G | 6609 | 6613 | 6610 | 6612 | −2 | 2 | $A_2$ |
| $^3F_4$ A | 6882 | 6886 | 6882 | 6872 | 10 | 13 | $B_1$ |
| B | 6885 | 6886 | 6885 | 6885 | 0 | 9 | $B_2$ |
| C | 6897 | 6902 | 6897 | 6894 | 4 | 17 | $A_2$ |
| D | 6901 | 6902 | 6901 | 6894 | 7 | 6 | $A_1$ |
| E | 7018 | | 7018 | 7019 | −1 | −4 | $A_1$ |
| F | 7024 | 7025 | 7024 | 7022 | 2 | 0 | $A_2$ |
| G | 7062 | 7061 | 7062 | 7046 | 16 | 12 | $B_2$ |
| H | 7075 | 7075 | 7075 | 7095 | −20 | −20 | $B_1$ |
| I | 7134 | | 7134 | 7144 | −10 | −25 | $A_1$ |
| $^1G_4$ A | 9725 | | 9725 | 9734 | −9 | 21 | $A_2$ |
| B | 9745 | | 9745 | 9753 | −8 | 15 | $A_1$ |
| C | 9872 | | 9872 | 9868 | 4 | 30 | $B_1$ |
| D | 9895 | | 9895 | 9889 | 6 | 46 | $B_2$ |
| E | 9991 | | 9991 | 10004 | −13 | −48 | $B_2$ |
| F | 10056 | | 10056 | 10077 | −21 | −25 | $A_2$ |
| G | 10056 | | 10056 | 10081 | −25 | −12 | $A_1$ |
| H | 10117 | | 10117 | 10091 | 26 | 29 | $B_1$ |
| I | 10241 | | 10241 | 10238 | 3 | −66 | $A_1$ |
| $^1D_2$ A | 16655 | 16656 | 16655 | 16653 | 2 | −18 | $A_1$ |
| B | 16815 | | 16815 | 16818 | −3 | −42 | $A_1$ |
| C | (16886) | | | 16917 | | | $A_2$ |
| D | 17166 | | 17166 | 17142 | 24 | 39 | $B_2$ |
| E | 17225 | | 17225 | 17255 | −30 | 21 | $B_1$ |
| $^3P_0$ A | 20716 | 20716 | 20716 | 20736 | −20 | −20 | $A_1$ |
| $^1I_6/^3P_1$ A | 21051 | | 21051 | 21044 | 7 | 15 | $B_1$ |
| B | 21051 | | 21051 | 21044 | 7 | 10 | $A_1$ |
| C | 21232 | | 21232 | 21209 | 24 | 25 | $A_2$ |
| D | 21271 | | 21271 | 21253 | 18 | 17 | $B_2$ |
| E | 21414 | | 21414 | 21412 | 2 | −2 | $B_1$ |
| F | (21427) | | 21427 | 21429 | −2 | 1 | $B_2$ |

**Table 5.** (Continued)

| term manifold cryst field level label[a] | exptl energy absorption | exptl energy emission | fitted energy[b] | calcd energy with CI[c] | $\Delta$[d] with CI | $\Delta$[d] without CI[e] | $C_{2v}$ irrep |
|---|---|---|---|---|---|---|---|
| $^1I_6/^3P_2$ G | 21505 | | 21505 | 21505 | 1 | 30 | $A_2$ |
| H | 21535 | | 21535 | 21519 | 16 | −22 | $A_1$ |
| I | 21571 | | 21571 | 21573 | −2 | −16 | $A_1$ |
| J | 21571 | | 21571 | 21584 | −13 | −17 | $A_2$ |
| K | | | | 21704 | | | $B_2$ |
| L | (21749) | | | 21765 | | | $B_1$ |
| M | | | | 22005 | | | $A_2$ |
| N | (22018) | | | 22011 | | | $A_1$ |
| O | | | | 22038 | | | $B_1$ |
| P | (22070) | | | 22041 | | | $B_2$ |
| Q | (22355) | | | 22317 | | | $A_1$ |
| R | (22413) | | | 22394 | | | $A_2$ |
| S | 22445 | | 22445 | 22473 | −28 | −28 | $B_2$ |
| T | 22528 | | 22528 | 22516 | 12 | 1 | $A_1$ |
| U | 22582 | | 22582 | 22588 | −6 | 5 | $B_1$ |
| $^1S_0$ A | | | | 47250 | | | $A_1$ |

[a] Levels are labeled A, B, ... in order of increasing energy for a given multiplet term. [b] Experimental energy, $E_{obs}$, used for data fits. [c] Calculation includes $4f^2/4f6p$ configuration interaction. [d] $\Delta = E_{obs} - E_{calc}$. [e] $4f^2$ energy level calculation without configuration interaction.

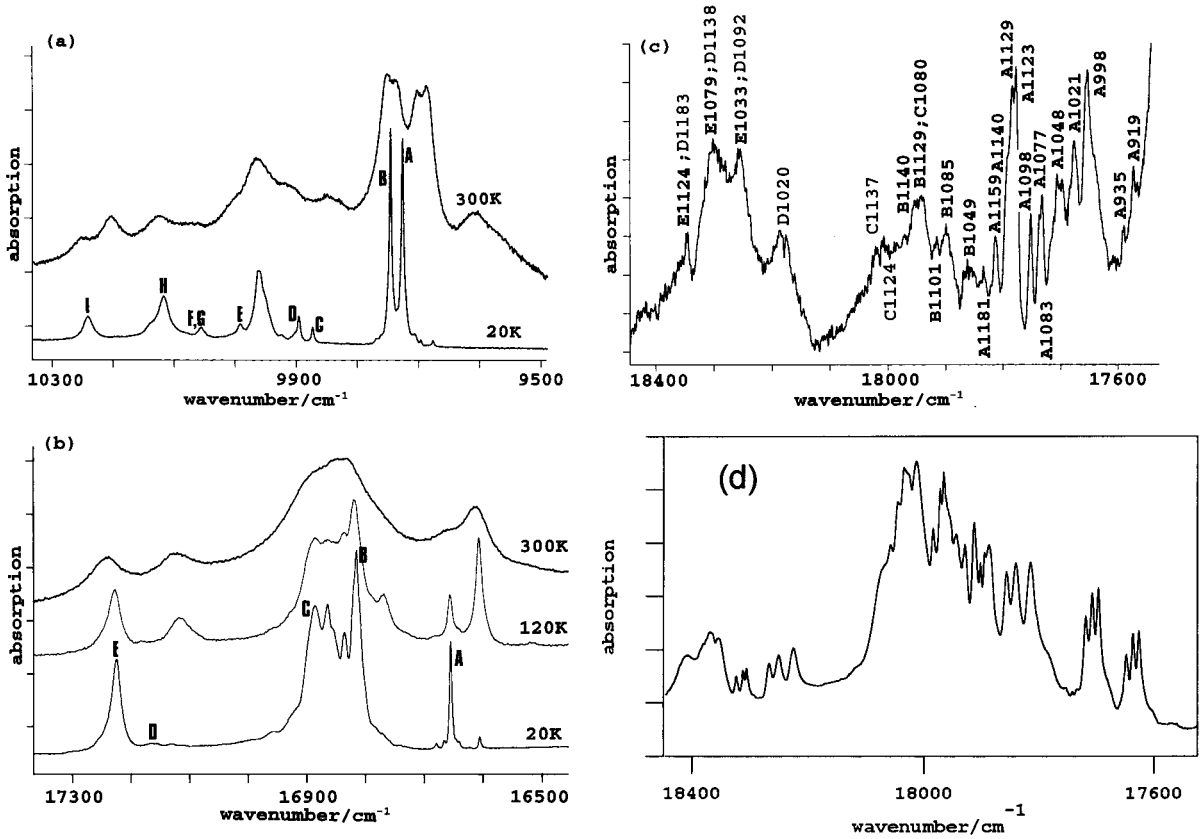


**Figure 6.** Absorption spectra of $Pr(H_2PO_2)_3$: (a) between 9500 and 10300 $cm^{-1}$ at 300 and 20 K; (b) 16500−17300 $cm^{-1}$ at 300, 120, and 20 K; (c) between 17550 and 18440 $cm^{-1}$ at 20 K; (d) simulated spectrum using product of 300 K infrared and 20 K zero phonon line absorption strengths (see section 3.7). In Figure 6a,b the labels A, B, ... refer to the terminal crystal field levels listed in Table 5. In Figure 6c the label A919 indicates that the structure is located at 919 $cm^{-1}$ to high energy of zero-phonon line A. Pressed disks were used for spectra 6a,b, and a polycrystalline sheet was used for 6c. The $^3H_4 \rightarrow {}^1D_2$ zero-phonon lines exhibited total absorption in 6c.

(Figure 3), and those at 138, 189, and 315 $cm^{-1}$ could correspond to electronic Raman transitions. The appearance of non totally symmetric Raman-active modes in the vibronic sideband of a centrosymmetric chromophore has previously been used as a criterion for the electric dipole allowed pure electronic transition.[58] In the case of $Pr(H_2PO_2)_3$, the energies of Raman-active modes are generally close to those of infrared-active modes, and nearly 20 bands are resolved between 50 and 320 $cm^{-1}$ in the Raman spectrum so that some (chance) coincidences with vibronic structure are likely. Thirteen weak features are resolved between 50 and 320 $cm^{-1}$ in the $^3H_4 \rightarrow {}^3P_0$ vibronic sideband, assigned to acoustic modes, lattice modes, and Pr−O stretch and bending modes.

A different situation is encountered, however, in the sidebands of the $^3H_4 \rightarrow {}^1G_4$ and $^3H_4 \rightarrow {}^1D_2$ transitions, where some strong, broad features are assigned to vibronic structure, with derived vibrational energies between 180 and 250 $cm^{-1}$, and maximum intensity near 210 $cm^{-1}$ (Figure 6a,b). Assuming the assignments to be correct, the reason why vibronic structure should appear

(58) Dickinson, J. R.; Piepho, S. B.; Spencer, J. A.; Schatz, P. N. *J. Chem. Phys.* **1972**, *56*, 2668.

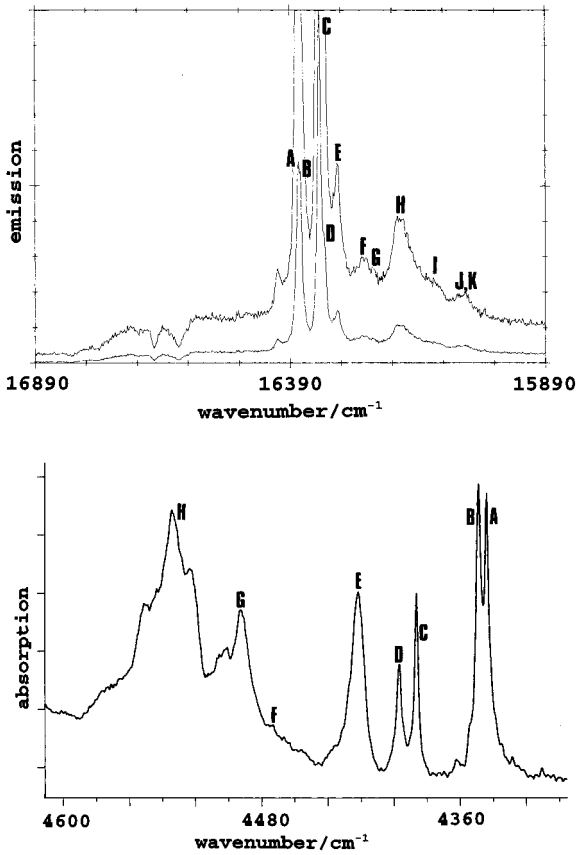


**Figure 7.** 80 K emission and 20 K absorption spectra of $Pr(H_2PO_2)_3$ with transitions terminating in the $^3H_6$ multiplet term. The labels A−K refer to the $^3H_6$ crystal field components listed in Table 5. The high-energy dips in the emission spectrum correspond to $^3H_4 \rightarrow {}^1D_2$ absorption transitions.

stronger in these particular transitions is interesting, and one possible mechanism is investigated here.

The dipole strength of the $q$th polarized component of the $A\alpha \rightarrow B\beta$ vibronic transition $D^q_{A\alpha,B\beta} = |P^q_{A\alpha,B\beta}|^2$, where[57]

$$P^q_{A\alpha,B\beta} = \langle A,\alpha|M^q|B,\beta\rangle \tag{2a}$$

$$= (A|M^q|B)(\alpha|\beta) - (A|M^q|C)(B|H'|C)(\alpha|Q|\beta)(E_C - E_B)^{-1} - (C|M^q|B)(A|H'|C)(\alpha|Q|\beta)(E_C - E_A)^{-1} + \{(A|M^q|A) - (B|M^q|B)\}(A|H'|B)(\alpha|Q|\beta)(E_B - E_A)^{-1} + ... \tag{2b}$$

where the integrals involving the initial (A), final (B), and intermediate (C) electronic states are over electronic coordinates and those of $\alpha$ and $\beta$ are over vibrational coordinates. $M^q$ is the $q$th component of the operator $M$, of which the electric dipole operator is the most important. $H'$ is the vibronic coupling operator acting on electronic states, and $Q$ is a 1-phonon operator, with the vibration labels $\alpha$ and $\beta$ referring to the $v = 0$ and $v = 1$ states, respectively, in the present low-temperature absorption study. As mentioned above, for intraconfigurational f−f transitions, the overlap integrals are small so that the first term in eq 2b may be neglected. The energy denominator ($E_B - E_A$) is typically 5−10 times smaller than ($E_C - E_A$) or ($E_C - E_B$). In eq 2b, and subsequently, rounded kets denote zeroth-order (vibronically unperturbed) states, for which the electronic states of $Pr^{3+}$ are intermediate coupling $4f^2$ states $|LSJ\Gamma_\gamma\rangle$, but which in the presence of opposite parity static crystal field terms may also comprise 4f5d states:

$$|B) = b|B[4f^2]\rangle + x|X[4f^2]\rangle + ... + b'|B'[4f5d]\rangle + ... \tag{3}$$

The coefficient $b'$ has been shown to be significant where B′ is $^1D_2$, since eigenvector mixing of the "$4f^2$ singlet" with the 4f5d term of up to 10% may occur.[59] In this case the so-called permanent contributions[57] in eq 2b, reflecting the difference between the electric dipole moments of states $|A) = {}^3H_4$ and $|B) = {}^1D_2$, will have the largest magnitude. These contributions could therefore account for the anomalously high vibronic intensities of some absorption transitions terminating in $^1D_2$. The opposite-parity mixing does not appear to be so important for $^1G_4$, however. The assignment of the strong vibronic structure in the absorption transitions to $^1G_4$ and $^1D_2$ might be further clarified from studies of isotopically substituted species.

Generally sharper features (fwhm 4−15 $cm^{-1}$) are observed in the infrared spectral region (< 10 000 $cm^{-1}$) than above 20 000 $cm^{-1}$ (fwhm 10−25 $cm^{-1}$) in the absorption spectrum of $Pr(H_2PO_2)_3$, and this appears to be the case for other $Pr^{3+}$ systems also. Inhomogeneous broadening makes the major contribution to line widths in $Pr(H_2PO_2)_3$. Either this is greater for the higher energy states or a vibronic contribution through acoustic modes from the first and fourth terms of eq 2b could be of importance, because these states are more strongly mixed with opposite-parity states. Broadening of structure to high energy of 20 000 $cm^{-1}$ in the absorption spectra of $Pr(CH_3COO)_3 \cdot H_2O$ has been attributed to ion pair interactions,[53] from the comparison of the vibronic sideband of this crystal with that of $Ce(CH_3COO)_3 \cdot H_2O$ doped with $Pr^{3+}$. Saturation effects make such intensity comparisons difficult. The probability for two ion processes is to first order, linearly proportional to the oscillator strengths of the individual ion processes, and is therefore small. Furthermore, similar broadening of bands in other spectral regions would occur if this mechanism were important.

**3.7. Two-Center Vibronic Transitions.** The one-center vibronic transitions involve $PrO_8$ moiety modes with vibrational energies below 400 $cm^{-1}$. For higher energy vibrational modes, a different type of vibronic transition is possible in $Pr(H_2PO_2)_3$ in which a vibrational hypophosphite moeity mode excitation occurs simultaneously with the $Pr^{3+}$ electronic transition. These two-center vibronic transitions comprised a major motivation for the present study of the electronic spectra of $Pr^{3+}$ situated at a site of low symmetry, because there are two spectral windows, (i) between the $^1G_4$ and $^1D_2$ transitions and (ii) between the $^1D_2$ and $^3P_0$ transitions, where P−H stretch vibronic structure can be studied under high sensitivity. However, coincident bands observed in these regions were found to correspond to electronic absorption transitions of $Nd^{3+}$ present as an impurity, and the spectra are described together with those of *neat* $Nd(H_2PO_2)_3$ in section 3.9.

Other regions for the study of these phenomena in the absorption spectra of $Pr(H_2PO_2)_3$ are more complex due to overlapping electronic transitions. Figure 6c shows part of the $^3H_4 \rightarrow {}^1D_2$ sideband in a thick polycrystalline sample of $Pr(H_2PO_2)_3$, in a region which does not overlap with the $Nd^{3+}$ impurity bands. The energies of bands are marked relative to those of the electronic origins A−E (Table 5). The current understanding of this type of transition is based upon Dexter−Stavola theory.

The theory of two-center vibronic transitions, as developed by Dexter and Stavola,[33] utilizes radiative dipole matrix elements with wave functions corrected for the electrostatic interaction,

(59) Garcia, D.; Faucher, M. *J. Chem. Phys.* **1989**, *90*, 5280.

$H_{AB}$, between electrons at center A and nuclei at center B. In the present work, center A corresponds to the $Pr^{3+}$ ion and center B to P−O or P−H nuclei. The electric dipole strength for the $q$th polarized component of the transition in which A undergoes an intraconfigurational $4f^2$ transition, $A_1 \rightarrow A_2$, and one quantum of vibration is simultaneously excited at center B, i.e., $B_1 \rightarrow B_2$, is

$$P^q_{A_1B_1,A_2B_2} = |\langle A_1B_1|M^q_A + M^q_B|A_2B_2\rangle|^2 \quad (4)$$

where $M_A$ and $M_B$ operate over the coordinates of A and B, respectively. Dropping the superscript $q$ in the following, assuming that $A_1$ and $B_1$ refer to ground states with reference energy zero, and denoting intermediate states by the subscript $u$, the matrix element in eq 4 is expanded:

$$\langle A_1B_1|M_A + M_B|A_2B_2\rangle = (A_1B_1|M_A + M_B|A_2B_2) \quad (5a)$$

$$-\sum_{u\neq 1}(A_u|M_A|A_2)(A_1B_1|H_{AB}|A_uB_2)(E_{A_u} + E_{B_2})^{-1} \quad (5b)$$

$$-\sum_{u\neq 2}(B_u|M_B|B_2)(A_1B_1|H_{AB}|A_2B_u)(E_{A_2} + E_{B_u})^{-1} \quad (5c)$$

$$-\sum_{u\neq 2}(A_1|M_A|A_u)(A_uB_1|H_{AB}|A_2B_2)(E_{A_2} + E_{B_2} - E_{A_u})^{-1} \quad (5d)$$

$$-\sum_{u\neq 1}(B_1|M_B|B_u)(A_1B_u|H_{AB}|A_2B_2)(E_{A_2} + E_{B_2} - E_{B_u})^{-1} \quad (5e)$$

The first term (5a) is nonzero in the presence of odd crystal field terms but was omitted by Stavola and Dexter[33] and has since been the subject of discussion.[34,36,37] Following several assumptions, such as the neglect of terms 5c and 5e and of interference effects when squaring matrix elements, and the restriction of $H_{AB}$ to dipole−dipole coupling interactions, and approximations such as the averaging over polarization directions and over LSJ-multiplet states of A, a simple expression for the dipole strength of the cooperative absorption $A_1B_1 \rightarrow A_2B_2$ was derived,[33]

$$P_{A_1B_1,A_2B_2} = (10e^4/3\kappa^2R^6)(2J+1)^{-1}\Xi^2(1,2) |(B_1|D_B|B_2)|^2|(A_1|U^{(2)}|A_2)|^2 \quad (6)$$

where

$$\Xi(1,2) = 2\Delta(n'l')^{-1}\sum_{n'l'} \begin{Bmatrix} 1 & 2 & 1 \\ f & l' & f \end{Bmatrix}(4f|r|n'l')^2(f||C^{(1)}||l')(l'||C^{(1)}||f) \quad (7)$$

and $D$ is the electric dipole operator, $U^{(2)}$ is a second rank unit tensor operator, $n'l'$ denotes other configurations with energy denominator $\Delta(n'l')$, and other symbols are defined in ref 33. Using eq 6, the magnitudes of matrix elements $(A_1|U^{(2)}|A_2)$ have been compared with two-center vibronic intensities in lanthanide ion systems, under the selection rule $\Delta J = 0, \pm 2$.[60,61] However, we note that eq 6 is a very crude approximation, and that higher order multipole−multipole interactions are important.[62] Indeed, the physical meaning of eq 6 is that the cooperative absorption transition probability is proportional to the electric quadrupole strength of the $A_1 \rightarrow A_2$ transition. Inspection of the master equations, 5b and 5d with rank 1 operators, shows that $P_{A_1B_1,A_2B_2}$ is in fact directly proportional to (i) the *electric dipole* intensity of the transition $A_1 \rightarrow A_2$ and (ii) the intensity of infrared absorption at center B in the transition $B_1 \rightarrow B_2$. In fact, the $U^{(2)}$ tensor appears in eq 6 as a result of the coupling of the two *lowest rank* operators in the multipole expansions of $M_A$ and $H_{AB}$. In the present study, we base our analysis upon these results i and ii from the master equations.

The similarity of the physical mechanism of the cooperative vibronic absorption to that of the Judd static odd-parity mixing was, in fact, recognized by Dexpert-Ghys and Auzel.[37] These authors also compared the cooperative vibronic transition mechanism with the Faulkner−Richardson mechanism[63] of the one-center vibrationally induced zero-phonon line intensity in centrosymmetric compounds. However, the vibronic intensity of one-center vibronic transitions at centrosymmetric sites depends upon vibrational integrals[64] and not upon vibrational dipole strengths.

Previous studies of cooperative vibronic transitions have estimated the cooperative transition oscillator strengths from assumed infrared dipole strengths and measured zero-phonon line oscillator strengths.[35−37] In the case of the $^2F_{5/2} - {}^2F_{7/2}$ $Yb^{3+}$ transitions, the latter may include an appreciable magnetic dipole contribution. The studies have been limited to OH group vibrational modes, with large bandwidths, so that the comparison of cooperative absorption strengths of different vibrational modes was not possible. Furthermore, previous studies have utilized room temperature electronic absorption spectra with broad spectral features.

The assignment of cooperative absorption bands has been made in Figure 6c. The region between 17 840 and 17 570 $cm^{-1}$ can be assigned to structure mainly built upon origin A. The derived energies of the $PH_2$ rock, twist, wag, and scissor modes and the $PO_2$ symmetric and antisymmetric stretch are similar to those in Table 3, from the infrared spectrum. Many of the relative intensities of the vibronic bands between 1000 and 1185 $cm^{-1}$ to high energy of electronic origin A follow a similar pattern to bands in the infrared spectrum, with the $PH_2$ wags being weaker than both the $PH_2$ scissor to higher energy and the $PO_2$ symmetric stretch to lower energy. No prominent vibronic feature is observed corresponding to the strongest band in the Raman spectrum in this region, at 1058 $cm^{-1}$, and the $PH_2$ twists are silent in the vibronic sideband. A closer examination, however, shows that the vibronic intensity pattern of the $PH_2$ scissor region does differ from that in the infrared spectrum, with the highest energy band being strongest in the infrared but weakest in the vibronic sideband. In Figure 6d a simulation of the cooperative vibronic absorption spectrum is presented, based on assumptions i and ii above, utilizing the 300 K infrared absorption spectrum and the zero-phonon line 20 K absorption strengths. The agreement is generally poor, partly because the zero-phonon lines B and C are much stronger than A, whereas vibronic structure based upon A is more prominent. In conclusion, the two-center vibronic sidebands of $Pr(H_2PO_2)_3$ are not ideal systems for study because the complexities of overlapping electronic transitions are present. Qualitative agreement is obtained, however, between the vibrational energies observed in the infrared absorption spectrum and the derived vibrational energies from the vibronic sidebands.

(60) Blasse, G. *Int. Rev. Phys. Chem.* **1992**, *11*, 71.
(61) de Mello Donega, C.; Meijerink, A.; Blasse, G. *J. Phys.: Condens. Matter* **1992**, *4*, 8889.
(62) Mason, S. F.; Peacock, R. D.; Stewart, B. *Mol. Phys.* **1975**, *30*, 1829.
(63) Faulkner, T. R.; Richardson, F. S. *Mol. Phys.* **1978**, *35*, 1141.
(64) Acevedo, R.; Tanner, P. A.; Meruane, T.; Poblete, V. *Phys. Rev.* **1996**, *B54*, 3976.

A quantitative model, in which the vibronic intensities are assumed to be proportional to the individual electric dipole strengths of both the appropriate vibrational *and* the pure electronic transitions, gives poor agreement with experiment. The experimental test of the model is discerning due to the large number of vibrational degrees of freedom in the crystal system. The reasons for the failure of the model are discussed in section 4.

**3.8. Crystal Field Calculations.** By contrast to the theories of spectral intensity where mixing of *opposite*-parity states ($4f^{n-1}Nd$, $4f^{n-1}Ng$, ...) is of utmost importance, the mixing with *the same* parity states is a mechanism by which the positions of calculated energy levels can be tuned in order to accurately match their experimentally measured values. One noticeable exception to this rule was the first case examined, that of (the Margolis dataset of) $PrCl_3$ which could be equally well fitted in a $4f^2/4f5d$ or in a $4f^2/4f6p$ scheme.[65] But, to date, the most efficient interacting configuration for adjustment purposes has been taken as $Nf^{n-1}(N+2)p$ in the cases of other systems of $Pr^{3+}$, $Nd^{3+}$, and $U^{4+}$.[28−30] Both the "classical" analysis of the experimental dataset in $4f^2$ and the simplest analysis[65] within an extended basis $4f^2/4f6p$ are presented here. The Hamiltonian which is utilized to solve the electronic structure of $Pr^{3+}$ in $Pr(H_2PO_2)_3$ is written as[66−68]

$$H = \Sigma F^k(\mathrm{f,f,f,f}) f_k + \zeta(f) A_{so} + \Sigma B_q^k(\mathrm{f,f}) C_q^k + \alpha L(L+1) + \beta G(G_2) + \gamma G(R_7) + \Sigma M^k m_k + \Sigma P^k p_k + \Sigma R^k(\mathrm{f,f,f,p}) g_k + \zeta(\mathrm{p}) A_{so} + \Sigma B_q^k(\mathrm{f,p}) C_q^k \quad (8)$$

The first eight terms in $H$ represent the usual interactions in $4f^2$, while the last three are the main anisotropic interactions with fp excited configurations. The $F^k$'s ($k = 0, 2, 4, 6$) are the Slater integrals and the $f_k$'s are the corresponding matrix elements. $\zeta$(f) is the spin−orbit coupling coefficient of the f electron. $\alpha$, $\beta$, and $\gamma$ are interconfiguration free-ion parameters. $G(G_2)$ and $G(R_7)$ are Casimir's operators for groups $G_2$ and $R_7$. The $M^k$'s ($k = 0, 2, 4$) and $P^k$'s ($k = 2, 4, 6$) are the coefficients of orbit−orbit and electrostatically correlated spin−orbit interactions, respectively.[69] The $B_q^k$(f,f) are the crystal field parameters (CFP) within $4f^2$. The effective free-ion operators associated with $\alpha$, $\beta$, and $\gamma$, the $M^k$'s and $P^k$'s, are applied within the ground configuration only. The last three terms concern configuration interaction: the $R^k$(f,f,f,p) ($k = 2$ and 4) are hybrid radial integrals involving $4f^2$ and 4f6p; and the $g_k$ are the associated operators. $\zeta$(p) is the spin−orbit coupling constant of the p electron. $B_q^k$(f,p) is a CFP linking an f electron in $4f^2$ and a p electron in 4f6p; $C_q^k$ is the associated operator.

The crystal field analysis of $Pr^{3+}$ in $Pr(H_2PO_2)_3$ relies not only on the experimentally determined energy level scheme (Table 5) but also on geometric considerations in the first coordination polyhedron of $Pr^{3+}$. The nearest $Pr^{3+}$ neighbors are a polyhedron of eight oxygen atoms at distances ranging from 2.408 to 2.584 Å. Due to the low site symmetry ($C_1$) of $Pr^{3+}$, the degeneracies of the states of the $4f^2$ configuration are completely lifted, and the maximum number (27) of nonzero complex CFP are allowed, i.e., for $k = 2, 4, 6$; $0 \le q \le k$.

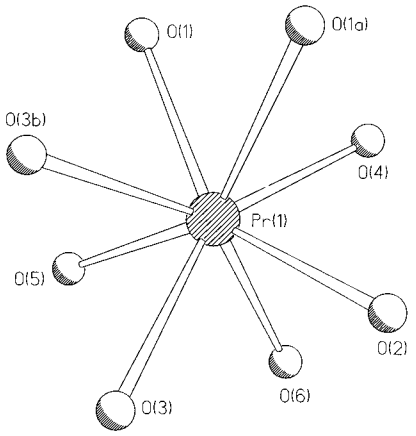


**Figure 8.** Projection of the eight oxygen ligands of $Pr^{3+}$ in $Pr(H_2PO_2)_3$ on a plane perpendicular to the pseudo-4-fold symmetry axis.

However, it is meaningless to fit such a large number of parameters. Besides, all the eigenfunctions of the crystal field Hamiltonian belong to the same irreducible representation (irrep) so that no experimental means are able to assess the assignments of the observed spectral lines.

The analysis is, however, facilitated by an important empirical observation. In a number of LSJ term manifolds, namely, $^3F_2$, $^3F_3$, $^3F_4$, $^1G_4$, and $^1D_2$, one sublevel, either at the bottom or at the top of the experimental set, is well separated, while the others are grouped two by two as slightly separated doublets. This lifting of degeneracy suggests the existence of a quasi second-order axis. It is noteworthy that, with a given set of CFP, it is possible to generate, by rotating the reference axes, an infinite number of other equivalent sets. It is therefore of interest to select as the quantization axis a direction along which a maximum of crystal field parameters cancel, making the crystal field fits easier and, above all, more reliable. Since the coordination polyhedron of $Pr^{3+}$ is a distorted square antiprism, a pseudo-4-fold axis of the antiprism seems to be a good choice. To bring the quantization axis along this direction, Pr(1) (at $x = 0.27073$, $y = 0.57864$, $z = 0.35781$) is chosen as the origin of coordinates. The Euler angles of the rotations are $\gamma = 48°$ around OZ, and $\beta = 34°$ around OV (perpendicular to OX in the OX, OY plane). Viewed along the OZ axis, the coordination polyhedron then looks like a distorted square antiprism. This is shown in Figure 8, which represents the projection of the eight oxygen ligands on a plane perpendicular to the pseudosymmetry axis. The covalo-electrostatic model[31] was utilized to calculate the theoretical crystal field parameters of $Pr^{3+}$ in this environment as well as in a perfect antiprism arrangement (Table 6, columns 4 and 5, respectively). In the latter case all the CFP vanish except $B_0^2$, $B_0^4$, and $B_0^6$. The similarities between both cases are striking: in $Pr(H_2PO_2)_3$, the calculated $B_0^k$'s are large and dwarf the other parameters. The consequence for the electronic sublevels should be the presence within each LSJ term manifold of weakly split doublets corresponding to $\pm M_J$ wave functions, and of one separate level corresponding to $M_J = 0$. This is experimentally observed as described above. In $^3F_2$, $^3F_3$, $^3F_4$, $^1G_4$, and $^1D_2$ it is thus possible to assign a level with a large proportion of $M_J = 0$ (and therefore a $C_{2v}$ ($A_1$ or $A_2$) level) at 5243, 6610, 7134, 10241, and 16655 $cm^{-1}$, respectively (Table 5). In $^3F_4$, the doublet structure is particularly pronounced. This information is invaluable for the assignment of energy levels.

Table 6 provides a set of theoretical starting CFP values for $Pr(H_2PO_2)_3$. If the parameters $<100$ $cm^{-1}$ are neglected, only $B_0^2$, $B_2^2$, $B_0^4$, $B_2^4$, $B_3^4$, $B_4^4$, $(S_4^4)$, $B_0^6$, $B_3^6$ and $B_4^6$, $(S_4^6)$ are left: i.e., 11

(65) Faucher, M. D.; Kooy, H. J. *Solid State Commun.* **1997**, *102*, 663.
(66) Judd, B. R. *Operator Techniques in Atomic Spectroscopy*; McGraw-Hill: New York, 1963.
(67) Wybourne, B. G. *Spectroscopic Properties of the Rare Earths*; Interscience: New York, 1965.
(68) Rajnak, K.; Wybourne, B. G. *Phys. Rev.* **1964**, *134*, A596.
(69) Crosswhite, H. M.; Crosswhite, H.; Kaseta, F. W.; Sarup, R. *J. Chem. Phys.* **1976**, *64*, 1981.

**Table 6.** Free-Ion and Crystal Field Parameters (CFP) of $Pr^{3+}$ in $Pr(H_2PO_2)_3$ with and without Configuration Interaction[a]

| | CFP value | | theor CFP(f,f) value | |
|---|---|---|---|---|
| param | from $4f^2/4f6p$ fit | from $4f^2$ fit | for $Pr(H_2PO_2)_3$ | for antiprism structure |
| $F^0$(f,f,f,f) | 12563 | 12346 | | |
| $F^2$(f,f,f,f) | 68749 | 68601 | | |
| $F^4$(f,f,f,f) | 50947 | 50508 | | |
| $F^6$(f,f,f,f) | 34111 | 33266 | | |
| $\alpha$ | 19.38 | 22.00 | | |
| $\beta$ | −614.9 | −650.2 | | |
| $M^0$ | 2.15 | 1.63 | | |
| $P^2$ | 343 | 401 | | |
| $\zeta$(f) | 746.2 | 742.9 | | |
| $B_0^2$(f,f) | −443 | −422 | −539 | −1006 |
| $B_2^2$(f,f) | −97 | −292 | −191 | |
| $B_0^4$(f,f) | −1603 | −1545 | −2346 | −2157 |
| $B_2^4$(f,f) | −161 | −202 | −521 | |
| $B_3^4$(f,f) | | | −500 | |
| $B_4^4$(f,f) | −219 | −222 | −257 | |
| $S_4^4$(f,f) | | | −257 | |
| $B_0^6$(f,f) | 819 | 951 | 1391 | 1815 |
| $B_3^6$(f,f) | | | −182 | |
| $B_4^6$(f,f) | −39 | −169 | −304 | |
| $S_4^6$(f,f) | | | −236 | |
| $X^2$ | 2.08 | | | |
| $X^4$ | 4.06 | | | |
| $B_0^4$(f,p) | −10304 | | | |
| $B_2^4$(f,p) | 6709 | | | |
| $B_4^4$(f,p) | −8061 | | | |
| $\delta$[b] | 11.9 | 20.6 | | |
| $\sigma$[c] | 14.0 | 23.0 | | |
| $N$ | 76 | 76 | | |
| $n_p$ | 21 | 16 | | |

[a] All energies are in $cm^{-1}$. The parameters $\gamma$ (1371 $cm^{-1}$) and $\zeta$(p) (3800 $cm^{-1}$) and the gap $F^0$(f,f,f,p)−$F^0$(f,f,f,f) (124343 $cm^{-1}$) were constrained. [b] Mean deviation, $\delta = (\sum_{i=1,N}(E_{i,obs} - E_{i,calc})^2/N)^{0.5}$. [c] Standard deviation, $\sigma = (\sum_{i=1,N}(E_{i,obs} - E_{i,calc})^2/(N - n_p))^{0.5}$.

parameters instead of 27 possible ones in $C_1$. Standard free-ion values were chosen as starting parameters. The $M^k$'s and $P^k$'s were linked by the relations $M^2/M^0 = 0.56$; $M^4/M^0 = 0.38$; $P^4/P^2 = 0.75$; $P^6/P^2 = 0.5$.[70] $\gamma$ was held constant, so that a total of nine free-ion parameters were employed in the $4f^2$ fit. When the data fit was carried out taking into account the above-mentioned assignments, $B_3^4$, $S_4^4$, $B_3^6$, and $S_4^6$ all rapidly approached zero. Therefore, only the remaining seven $C_{2v}$ (f,f) parameters $B_0^2$, $B_2^2$, $B_0^4$, $B_2^4$, $B_4^4$, $B_0^6$, and $B_4^6$ in $4f^2$ were retained, i.e., a total of 16 for the $4f^2$ calculation. For the calculation including the 4f6p configuration, $\zeta$(p) was held constant, and two additional free-ion parameters ($R^2$(f,f,f,p) and $R^4$(f,f,f,p)) as well as four additional CFP(f,p) ($B_0^2$, $B_0^4$, $B_2^4$, and $B_4^6$) were introduced. $B_0^2$ canceled spontaneously so that configuration interaction introduced five extra parameters, making a total of 21.

Seventy-six levels were introduced in the fitting process. The uncertain levels (not included in the column "fitted energy", Table 5) were omitted. The best fits in $4f^2$ and 4f6p yielded experimental/calculated mean deviation equal to 20.4 and 11.9 $cm^{-1}$, respectively. The final CFP are reported in Table 6 as well as the corresponding standard deviations which are equal to 23 and 14 $cm^{-1}$, respectively. If the uncertain levels are utilized as well, which makes a total of 83, the mean deviations climb up to 23 and 14 $cm^{-1}$ (and the standard deviations up to 26 and 16 $cm^{-1}$) in $4f^2$ and 4f6p, respectively. Practically, only the $C_{2v}$ CFP remain and, moreover, the $q \neq 0$ parameters are small so that the leading parameters are the $B_0^k$. The final calculated energy values are listed in Table 5 with the experimental values and the corresponding $C_{2v}$ irreducible representations. In the new axis coordinates, perfect doublets would correspond to $\pm M_J$ wave functions with sequences ($B_1$, $B_2$), ($A_1$, $A_2$), and a separate $A_1$ (or $A_2$) if $J$ is even (or odd). This structure is well respected in $^3F_3$, $^3F_4$, but not in $^1D_2$.

The $k = 2$ fitted parameters match well the predicted values, but those with $k = 4$ and 6 are about 1.5 times smaller. The global mean improvement which results from the utilization of a larger basis amounts to 39%. The mean deviations within the LSJ levels as well as the relative improvements are reported in Table 7. The largest fitting improvement is found in $^1G_4$ (58%), the less improved levels being $^3H_4$, $^3F_4$, and $^3P_2$ in the present case of $Pr(H_2PO_2)_3$.

**3.9. Absorption Spectrum of $Nd(H_2PO_2)_3$.** The $Nd^{3+}$ trace impurity present in our samples of $Pr(H_2PO_2)_3$ was identified from the absorption spectrum of $Nd(H_2PO_2)_3$. Figure 9 compares two groups of bands in the neat and diluted materials. Well-resolved hot bands arising from thermally excited crystal field levels B, C, and D of the $^4I_{9/2}$ ground state multiplet are readily observed between 30 and 120 K and are a valuable aid in the assignment of the energy levels. Table 8 shows that the derived energy level scheme for $Nd^{3+}$ is very similar to that of $NdCl_3 \cdot 6H_2O$, in which the structure is made up of $[Nd(H_2O)_6Cl_2]^+$ and $C1^-$ ions, with the $Nd^{3+}$ ion also being 8-coordinate, but in a distorted triangulated dodecahedron.[71] The crystal field levels are therefore unable to "fingerprint" the given type of coordination environment,[71] but may be useful in predicting the lanthanide coordination number. The $Ln^{3+}$ ion is situated at a $C_2$ site in the monoclinic hexahydrated lanthanide trichlorides, but optical spectra have been interpreted under higher point group symmetry in some cases.[72] It is apparent from Table 8 that the electronic degeneracies of all crystal field levels of $Nd^{3+}$ are completely removed. For an odd-electron system, this is compatible with a site symmetry lower than cubic symmetry. The crystal field splittings of the multiplet terms are slightly smaller in the case of the $NdCl_3 \cdot 6H_2O$, compared with $Nd(H_2PO_2)_3$, because two oxygen nearest neighbors have been replaced by chlorines. The crystal field splittings are even smaller, and the energy level scheme is very different for $LaCl_3$:$Nd^{3+}$, where the cation is 9-coordinate to chlorine.[73]

## 4. Summary and Conclusions

Both of the anhydrous and monohydrated lanthanide hypophosphite complexes form three-dimensional chain structures, with hypophosphite groups acting as links. In $Pr(H_2PO_2)_3$, the shortest Pr−Pr distances (4.193, 4.271 Å) are shorter than in $Pr(CH_3COO)_3 \cdot H_2O$. The vibrational spectra tend to confirm the arrangement and site symmetry of hypophosphite anions within the unit cell.

The electronic absorption and emission spectra confirm that only one type of lanthanide ion is present, and that the site symmetry is $C_2$ or lower. Possible contributions from the so-called permanent terms (fourth term, 2b) and Franck−Condon term (first term, 2b) in the electronic absorption spectra of Pr-

(70) Crosswhite, H. M.; Crosswhite, H. *J. Opt. Soc. Am. B* **1984**, *1*, 246.
(71) Stump, N. A.; Schweitzer, G. K.; Gibson, J. K.; Haire, R. G.; Peterson, J. R. *Appl. Spectrosc.* **1994**, *48*, 937.
(72) Harrop, I. H. *J. Chem. Phys.* **1965**, *42*, 4000.
(73) Morrison, C. A.; Leavitt, R. P. In *Handbook on the Physics and Chemistry of Rare Earths*; Gschneidner, K. A., Eyring, L., Eds.; North-Holland: Amsterdam, 1982; Chapter 46.

**Table 7.** Global Mean Deviations, $\delta$, and Those within Selected Term Manifold Levels, between Experimental and Calculated Energy Levels for $Pr(H_2PO_2)_3$ and $Cs_2NaPrCl_6$[a]

| | | | term manifold mean deviation, $\delta$ | | | | | | | | |
|---|---|---|---|---|---|---|---|---|---|---|---|
| $Pr^{3+}$ system | type of calcn | $\delta$ | $^3H_4$ | $^3H_5$ | $^3H_6$ | $^3F_2$ | $^3F_3$ | $^3F_4$ | $^1G_4$ | $^1D_2$ | $^3P_2$ |
| $Pr(H_2PO_2)_3$ | $4f^2/4f6p$ | 12 | 11 | 9 | 12 | 11 | 4 | 10 | 15 | 19 | 14 |
| | $4f^2$ | 20 | 15 | 17 | 18 | 20 | 7 | 14 | 36 | 32 | 18 |
| $Cs_2NaPrCl_6$[b] | $4f^2/4f6p$ | 13 | 7 | 14 | 6 | 4 | 8 | 31 | 7 | 5 | 5 |
| | $4f^2$ | 35 | 25 | 40 | 22 | 16 | 15 | 34 | 71 | 46 | 15 |

[a] All values in $cm^{-1}$. [b] Reference 32.

**Table 8.** Comparison of Energy Levels of $Nd(H_2PO_2)_3$ and $NdCl_3 \cdot 6H_2O$[a]

| | energy/$cm^{-1}$ of crystal field level | |
|---|---|---|
| term | $Nd(H_2PO_2)_3$[b] | $NdCl_3 \cdot 6H_2O$[c] |
| $^4I_{9/2}$ | A 0; B 76; C 132; D 221; E nd[d] | A 0 |
| $^4F_{3/2}$ | A 11442; B 11529 | A 11457; B 11531 |
| $^4F_{5/2}, ^2H_{9/2}$ | A 12453; B 12509; C 12538; D 12574; E 12630; F 12659; G 12704; H 12754 | A 12475; B 12509; C 12540; D 12571; E 12618; F 12674; G 12705; H 12739 |
| $^4F_{7/2}, ^2S_{3/2}$ | A 13405; B 13462; C 13516; D 13570; E 13579; F 13589 | A 13409; B 13484; C 13524; D 13567; E 13578; F 13586 |
| $^4F_{9/2}$ | A 14672; B 14719; C 14771; D 14794; E 14893 | A 14687; B 14732; C 14769; D 14807; E 14862 |

[a] Crystal field levels of a given multiplet term are labeled A, B, ... in order of increasing energy. [b] 20 K absorption, this study. [c] Reference 73. [d] Not determined.

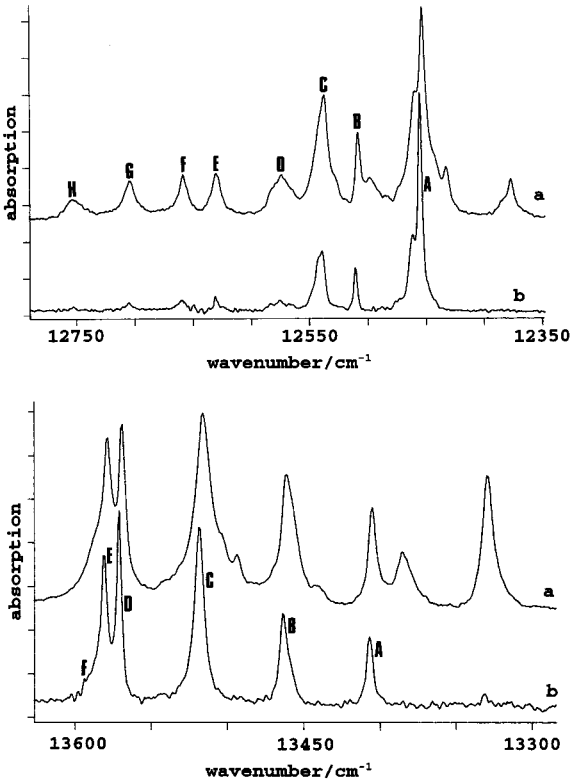


**Figure 9.** Comparison of (a) 100 K fluorolube mull absorption spectrum of neat $Nd(H_2PO_2)_3$ with (b) 20 K absorption spectrum of polycrystalline sheet of $Pr(H_2PO_2)_3$ between 12350 and 12780 $cm^{-1}$ and between 13300 and 13600 $cm^{-1}$. The labels A−H and A−F refer to the terminal crystal field levels of $^4F_{5/2}$, $^2H_{9/2}$ and $^4F_{7/2}$, $^2S_{3/2}$, respectively, Table 8.

$(H_2PO_2)_3$ have been discussed. Although the study of two-center vibronic transitions is largely not feasible for $Pr(H_2PO_2)_3$ because features are obscured by those from a trace impurity of $Nd^{3+}$, the simulation of the $^3H_4 \rightarrow {}^1D_2$ cooperative vibronic spectrum shows that the exclusive use of 5b and 5d does not give good agreement with experiment. In addition, the relative intensities of bands in the electronic spectra, corresponding to hypophosphite modes derived from the same free $H_2PO_2^-$ ion parent mode, differ from those in the infrared spectrum. The poor agreement could result from the omissions of the following considerations. The term 5a includes the Franck−Condon patterns based upon zero-phonon lines; and terms 5c and 5e include interactions such as $Pr^{3+}$ quadrupole−hypophosphite dipole, etc., so that even parity vibrational modes are then allowed in the vibronic sideband. An additional mechanism for cooperative vibronic transitions, not considered previously, is the mixing of symmetry coordinates of the external modes with those of first coordination sphere ($PrO_8$) vibrations. In physical terms, the cooperative vibronic sideband represents a "local infrared spectrum".[34] This is because the $A_u$ ($C_i$) unit cell group modes appear in the infrared spectrum, but the linear combination of hypophosphite modes transforming under the $C_1$(A) site irreducible representation at the $Pr^{3+}$ ion appear in the electronic absorption spectrum. The $PH_2$ and $PO_2$ modes will be further investigated in the vibronic sidebands of other $Ln(H_2PO_2)_3$ systems which do not present the complications of overlapping transitions and impurity bands, and for which single crystals can be obtained.

Theoretical CFP have been found to be in reasonable agreement with those from the experimental data fit. The energy level data fit is improved throughout by the inclusion of configuration interaction of $4f^2$ with 4f6p. The electronic energy level fit for $Pr^{3+}$ has been shown to be feasible under $C_{2v}$ rather than $C_1$ site symmetry of $Pr^{3+}$, although the consequent spectral selection rules for $C_{2v}$ irreps of excited states are not adhered to in the electronic spectra. In the ideal antiprism case ($D_{4d}$), only transition representations $\Gamma_i \times \Gamma_f$ of $E_1$ or $B_2$ transform in the same symmetry as the electric dipole moment operator, and the transition intensities derive from the imaginary component of the CFP $B_4^5$ ($S_4^5 \sim 2000$ $cm^{-1}$) and are expected to be small. The distortion from the ideal to the actual $Pr^{3+}$ symmetry in $Pr(H_2PO_2)_3$ introduces significant $B_q^k$ ($k$ odd) CFP, which are null in $C_{2v}$ symmetry. The spectral intensities are thus governed by the $C_1$ site symmetry odd CFP. By contrast, the energy levels in the ideal antiprism case are slightly perturbed in $Pr(H_2PO_2)_3$ by $C_{2v}$ site symmetry $B_0^k$ ($k$ even) CFP.

With the exception of $B_4^6$ and $B_2^2$, the CFP(f,f) do not change greatly upon the introduction of the excited configuration (Table 6). As in the case of $LiYF_4:Pr^{3+}$,[28] the fitted CFP(f,p) for $Pr(H_2PO_2)_3$ are not found to be proportional to the fitted CFP(f,f). If this *were* true, then it would considerably lower the number of CFP's in the energy level fitting process.

**Acknowledgment.** We thank Mr. Liu Yulong for recording the Raman and emission spectra; Mr. J. Krishnan, Ms. C. S.-K. Mak, and Mr. Pei Zhi Wu for technical assistance, Drs. T. J. R. Weakley and R. Kresinski for useful correspondence; the HK RGC for financial support under CUHK 303/96P and CPHK 229/92E; and SRG 7000762.

**Supporting Information Available:** Two X-ray crystallographic files, in CIF format. This material is available free of charge via the Internet at http://pubs.acs.org.

IC990187Z